

Increasing Large Wildfires over the Western United States Linked to Diminishing Sea Ice in the Arctic

Yufei Zou (✉ yufei.zou@pnnl.gov)

Pacific Northwest National Laboratory <https://orcid.org/0000-0003-2667-0697>

Philip Rasch

Pacific Northwest National Laboratory <https://orcid.org/0000-0002-5125-2174>

Hailong Wang

Pacific Northwest National Laboratory <https://orcid.org/0000-0002-1994-4402>

Zuwei Xie

Institute of Atmospheric Physics

Rudong Zhang

Pacific Northwest National Laboratory

Article

Keywords: large wildfires, anthropogenic climate change, Arctic sea ice, climate model sensitivity experiments

Posted Date: March 9th, 2021

DOI: <https://doi.org/10.21203/rs.3.rs-185815/v1>

License:   This work is licensed under a Creative Commons Attribution 4.0 International License.

[Read Full License](#)

Version of Record: A version of this preprint was published at Nature Communications on October 26th, 2021. See the published version at <https://doi.org/10.1038/s41467-021-26232-9>.

Title: Increasing Large Wildfires over the Western United States Linked to Diminishing Sea Ice in the Arctic

Authors: Yufei Zou^{1*}, Philip J. Rasch¹, Hailong Wang^{1*}, Zuowei Xie² & Rudong Zhang¹

Affiliations:

¹Atmospheric Sciences and Global Change Division, Pacific Northwest National Laboratory, Richland, WA 99354, USA.

²International Center for Climate and Environment Sciences, Institute of Atmospheric Physics, Chinese Academy of Sciences, Beijing, 100029, China.

*Correspondence to: Y. Zou (yufei.zou@pnnl.gov) and H. Wang (hailong.wang@pnnl.gov).

Abstract: The compound nature of large wildfires affected by multiple natural and anthropogenic factors in combination with complex interactions involved in hydroclimate-related physical processes make it difficult to directly connect wildfire changes over fire-prone regions like the western United States (U.S.) with anthropogenic climate change. Here we show that increasing large wildfires during autumn over the western U.S. are fueled by more fire-favorable weather associated with rapid declines in Arctic sea ice during preceding months on both interdecadal and interannual time scales. Our analysis (based on observations, climate model sensitivity experiments, and a multi-model ensemble of climate simulations) demonstrates and explains the Arctic-driven teleconnection through circulation changes with the poleward-shifted North Pacific jet stream and enhanced fire-favorable surface weather conditions. The amplitude of the Arctic-driven fire weather change is of similar magnitude to other leading modes of climate variability such as the El Niño-Southern Oscillation (ENSO) that also influence fire weather in the western U.S.

Main Text:

Large wildfires are an increasing threat to society and ecosystems over the western U.S., especially across the expanding wildland-urban interface (WUI) regions¹. Both numbers and total burned areas of large wildfires in this region have been increasing in the past few decades^{2,3}, causing a tremendous socioeconomic burden in terms of devastating casualties and losses, soaring fire prevention and suppression costs, and rising public health risk due to short-term and long-term fire smoke exposure^{4,5}. To understand the driving forces of this alarming trend, many studies have investigated its relationship with human activity^{6,7} and anthropogenic climate change⁸⁻¹⁰ from various perspectives. Unfortunately, the complexity of these interactions among human and natural dimensions of fire activity in the presence of natural variability in the climate system confounds the detection and attribution of changes in large wildfires over this region. Understanding these compound extreme weather events requires a multidisciplinary analysis framework across multiple spatiotemporal scales¹¹. Previous studies have suggested that climate impacts on regional fire activity might be masked by human influence on fire ignition and suppression, land use change, and forest management, implying complex human-climate-fire interactions where human impacts often prevail^{6,7}. However, for other wildland regions that are less affected by human activity, anthropogenic climate change still exerts dominant impacts on fire by increasing lightning ignitions in boreal forests¹² and modulating either fuel availability in resource-limited fire regimes (e.g., xeric shrublands and grasslands/savannas) or fuel aridity in condition-limited fire regimes (e.g., tropical and subtropical forests) where there is ample fuel supply¹³. Different characteristic scales of anthropogenic and natural processes also shed light on disentangling the fire-centered nexus between human and climate systems for extreme event detection and attribution. For instance, land use change and forest management with excessive

fire exclusion and human suppression better explains a forest “fire deficit” in the western U.S. decoupled from climate and fire weather changes on centennial time scales since the middle 1800s, while the reconciled trends of increasing large fires and worsening fire weather in recent decades suggest an increasingly important role of anthropogenic climate change in modulating regional fire activity on shorter (interannual to interdecadal) time scales¹⁴ as discussed here.

Fire weather variables such as temperature and precipitation provide strong explanatory power for seasonal to multidecadal fire activity in empirically-based statistical models that utilize such climate-fire relationships across the western U.S.^{2,6,9,10} as well as other fire-prone regions worldwide^{13,15-17}. However, a clear causal relationship with process-level understanding of complex climate-fire interactions cannot be drawn from these empirical models; those explanations are better provided by physically-based Earth system models (ESMs) with interactive fire components. In recent years, fire modeling in ESMs has advanced rapidly using various levels of model complexity to represent fire-related climate and vegetation processes¹⁸. These fire-enabled ESMs provide new tools for understanding the role of anthropogenic climate change on global and regional fire activity based upon process-level physical and ecological pathways. Here we use a state-of-the-art fire model with improved regional climate-fire interactions embedded in the Community Earth System model (CESM-RESFire)¹⁹ to investigate the linkage between worsening fire hazards in the western U.S. and the rapid sea-ice decline in the Arctic over the past four decades. The Arctic sea ice has been declining dramatically since the late 1970s particularly in summer and autumn, which is closely related with much stronger warming in the Arctic than the global mean temperature as so called Arctic amplification (AA)^{20,21}.

Our exploration of this sea ice-fire teleconnection has been motivated by increasing but still controversial evidence of emerging connections between high-latitude environmental change and mid-latitude weather extremes in both warm and cold seasons of the past few decades²¹⁻²³. Several studies have shown significant influence of Arctic sea-ice loss on regional fire weather conditions such as surface air temperature and precipitation based on global and regional climate models²⁴⁻²⁷ or even annual wildfire activity in the western U.S. based on statistical analysis²⁸, but a quantitative and mechanistic evaluation of the Arctic impact on regional burning and its comparison with other major climate modes is still lacking. Our observation-based statistical analysis (see Methods) also suggests a strong negative correlation ($r=-0.68$; p value <0.01) between declining sea-ice concentrations (SIC) over the Pacific sector of the Arctic (120 °E to 135 °W; 70 °N to 80 °N) in preceding summer and autumn (July to October) and worsening fire weather conditions (as described by a Fosberg Fire Weather Index²⁹, hereafter FFWI, based on the fifth generation of the European Centre for Medium-Range Weather Forecasts (ECMWF) atmospheric reanalysis of the global climate (ERA5)³⁰; see Methods) during the following autumn and early winter (September to December) over the western U.S. (124 °W to 97 °W; 32.5 °N to 48 °N; Fig. 1a, b). Changes in composite analyses between years with minimum (hereafter SIC-) and maximum (hereafter SIC+) sea-ice concentrations (marked with triangles in Fig. 1b) in the satellite era further reveals the existence of enhanced fire-favorable regional weather conditions as well as expanded burned area of large wildfires following Arctic sea-ice decline (Fig. 1c). This correlation is insensitive to the removal of long-term trends in Arctic SIC and regional FFWI ($r=-0.50$ with p value <0.01 after detrending; Supplementary Fig. 1), suggesting a statistically robust linkage between the Arctic sea ice and regional fire weather changes across interannual to interdecadal time scales. Results are also statistically significant

and robust when other reanalysis data products and fire weather indices are used (Supplementary Fig. 2), raising two questions to be addressed in this work: (1) What is the physical mechanism underlying this Arctic-originated teleconnection suggested by robust statistical correlations on different time scales? (2) How important is this teleconnection comparing to the general global warming effect as well as other teleconnections associated with major climate modes such as ENSO in the past four decades?

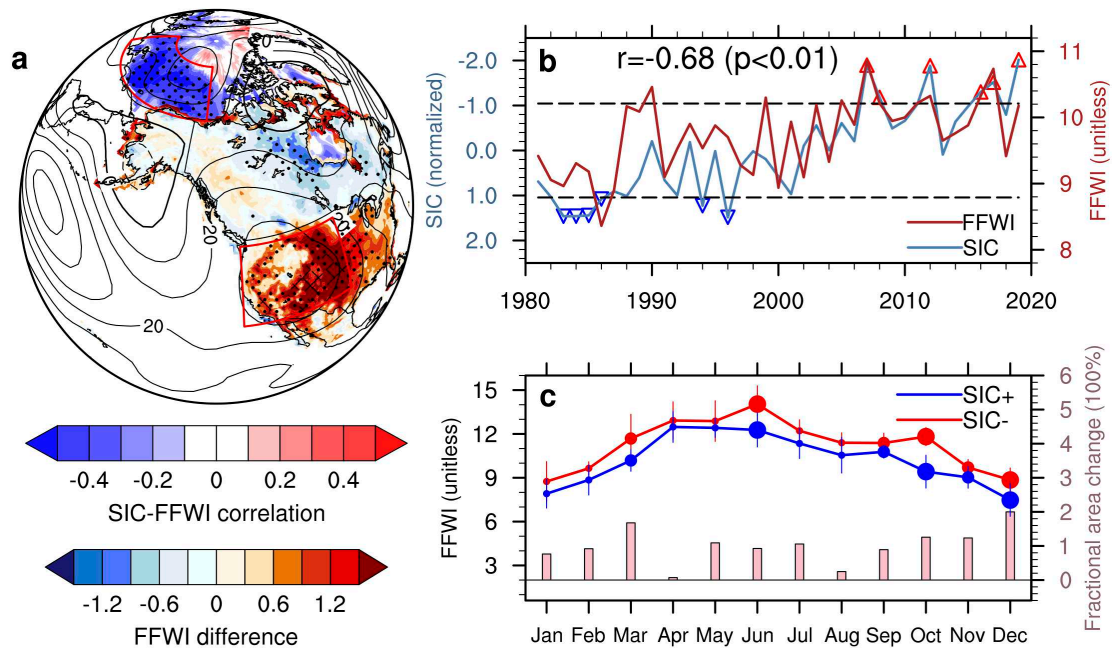


Fig. 1. Observation- and reanalysis-based Arctic sea ice and regional fire teleconnection. **a**, spatial distributions of the correlation (shading in the Arctic) between seasonal average Arctic sea-ice concentrations in summer and autumn (July to October) and seasonal and regional average FFWI over the western U.S. in the following autumn and early winter (September to December), and the difference of seasonal average FFWI (shading in the U.S.) between years with minimum (SIC-: red up-pointing triangles in **b**) and maximum (SIC+: blue down-pointing triangles in **b**) Arctic SIC. The difference of seasonal (September to December) average geopotential height at 500 hPa between the SIC- and SIC+ years is also shown (contours with negative values in dashed lines; unit: m). **b**, time series of seasonal and regional average SIC (seasonal mean from July to October; normalized by its 1981-2010 climatological mean and standard deviation), FFWI (seasonal mean from September to December), and their

correlation. The region definitions for the Pacific sector of the Arctic and the western U.S. are outlined by red boxes in **a**. The horizontal dashed lines denote the ± 1 standard deviations of normalized SIC as thresholds for selecting the SIC \pm years. **c**, the composite of monthly FFWI (solid lines with dots and error bars) and fractional burned area change of large wildfires (vertical bars) over the western U.S. Error bars in **c** denote ± 1 standard deviations of monthly FFWI in each group. Stipples in **a** mark regions that are significantly different from 0 at the 0.05 significance level of two-sided t-test, and hatching in **a** denotes statistically significant regions based on the stricter FDR method (see Methods) with local gridded p value $\leq p_{FDR}^* = 0.0023$ at the threshold of $\alpha_{FDR} = 0.10$. Dot sizes for monthly FFWI in **c** denote the 0.05 (large) and 0.1 (medium) significance levels of two-sided t-test, respectively.

To answer the first question, we have designed and conducted two climate model sensitivity experiments by prescribing perturbations to the regional Arctic sea-ice concentrations (Fig. 2a) and associated sea surface temperature (SST) corresponding to the minimum (hereafter SICexp-) and maximum (hereafter SICexp+) SIC conditions in the CESM-RESFire model to isolate the impact of Arctic sea-ice loss on regional fire weather and burning activity (see Methods). The modeling results show an anomalous dipole pattern in the 500 hPa geopotential height field averaged over September-December (hereafter Z500) with cyclonic (negative) anomalies centered over Alaska and anticyclonic (positive) anomalies centered over the western U.S. (Fig. 2a) in response to sea-ice reduction in preceding July to October. This anomalous circulation pattern is similar to that revealed by differencing reanalysis-based composites for the SIC- and SIC+ years constructed from the ERA5 data (Fig. 1a). The similarity is even more striking over the downstream North America continental regions when the SIC, FFWI, and burned area time series as well as gridded reanalysis data are all detrended by removing their long-term trends associated with global warming effects before differencing the new groups of years with minimum (hereafter SICnotrd-) and maximum (hereafter SICnotrd+) sea-ice concentrations in the detrended SIC time series (Supplementary Fig. 1a; see Methods). The improved similarity

between the modeling results and the detrended reanalysis data is understandable because there is also no global warming effect in the simulations other than those deliberately exposed using the Arctic sea ice-driven warming effect by differencing the SICexp- and SICexp+ experiments. Since the sea-ice forcing used in the climate model sensitivity experiments results from both interannual and interdecadal changes, we use both the original sea-ice and reanalysis data that include short-term and long-term variability and the detrended data that include interannual variability only for the following composite analyses to test the robustness of the composite results on different time scales. Note that the SIC-/+ (Fig. 1b) and SICnotrd-/notrd+ (Supplementary Fig. 1b) years are different for the two observation-/reanalysis-based composite analyses because of different SIC time series for composite member selection. We project the simulated Z500 anomalies onto a fire-favorable regional circulation pattern to obtain its corresponding time series (hereafter Z500i) in each experiment (see Methods). The statistical distributions of Z500i suggest a positive shift in SICexp- (Fig. 2b; p value=0.01) characterized by increased downward motion, suppressed clouds and precipitation, and increased incoming solar radiation over the western U.S. (Supplementary Fig. 3), contributing to a positive shift of regional FFWI (Fig. 2b; p value=0.06) with more frequent and intensified hot and dry surface weather conditions in autumn and early winter. Accordingly, such fire-favorable weather is conducive to regional fire activity with expanded burned area (Fig. 2a, c; p value=0.04) induced by both increased fire ignitions (Fig. 2d; p value=0.04) and enlarged fire sizes (Fig. 2e; p value<0.01). A month-by-month comparison between SICexp- and SICexp+ also shows consistent changes in regional fire weather, fire ignition, fire size, and total burned area in consecutive months after Arctic sea ice declining, with the largest increase of regional total burned area by ~12.5% in November (Supplementary Fig. 4). Besides the ensemble mean

responses, we also examine the probability and intensity changes of extreme burning years (defined by regional total burned area) using a bootstrap resampling method (see Methods). The results show dramatic increases with nearly four times higher occurrence probability and 14-15% higher burning intensity of extreme burning years under the SICexp- condition than that under the SICexp+ condition (Supplementary Fig. 5). This significant increase in the occurrence probability of extreme burning years is robust for both bootstrapping estimates without and with sample replacement after the modeling ensemble size exceeds 30 years (Supplementary Fig. 6).

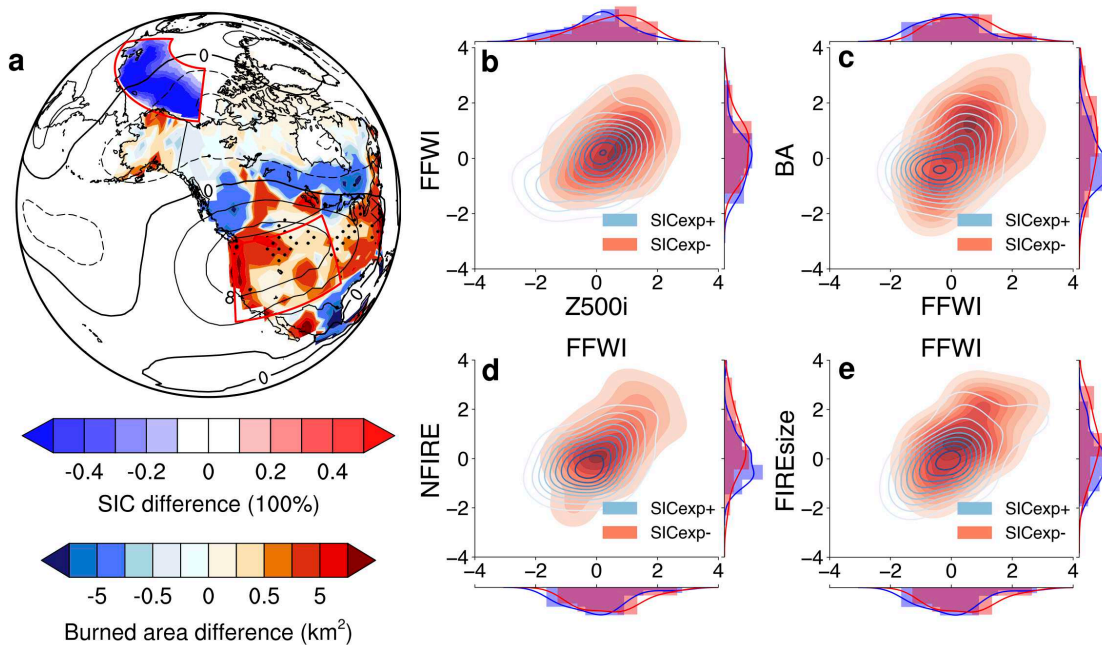


Fig. 2. CESM-RESFire simulated Arctic sea ice and regional fire teleconnection. **a**, spatial distributions of the seasonal average (July to October) sea-ice concentration difference (color shading in the Arctic Ocean) between the SICexp- and SICexp+ experiments, and the seasonal average (September to December) burned area change (color shading in North America) in response to the sea-ice perturbation. The difference of Z500 between SICexp- and SICexp+ is also shown (contours with negative values in dashed lines; unit: m). **b**, 2-dimensional distributions of the seasonal mean fire-favorable circulation index (Z500i; standardized by first removing the 40-year mean and then normalizing by the standard deviation of Z500i from the SICexp+ experiment) and FFWI (also standardized by the 40-year mean and standard deviation of FFWI from the SICexp+ experiment) based on the kernel density estimation

(KDE) for SICexp- (red shading) and SICexp+ (blue contours). 1-d KDE distributions for each index in SICexp- (red) and SICexp+ (blue) are also shown along the x- and y-axis. **c**, As in **b**, but for the comparison of standardized FFWI and regional burned area (BA). **d**, As in **b**, but for the comparison of standardized FFWI and regional mean fire count (NFIRE). **e**, As in **b**, but for the comparison of standardized FFWI and regional mean fire size (FIREsize). Stipples in **a** show regions that are significantly different from 0 at the 0.1 significance level of two-sided t-test, and hatching in **A** denotes statistically significant regions based on the stricter FDR method (see Methods) with local gridded p value $\leq p_{FDR}^* = 0.017$ at the threshold of $\alpha_{FDR} = 0.20$.

Additional diagnostics of atmospheric dynamics and thermodynamics help to better understand the physical processes contributing to the above sea ice-driven fire expansion. The observationally-based difference in zonally-averaged temperature (from the ERA5 reanalysis product) between SIC- and SIC+ years shows strong but heterogeneous warming both near the surface and in the free troposphere over mid- and high-latitude regions, manifested by an enhanced (reduced) meridional temperature gradient around 60 °N (80 °N) in the lower and middle troposphere (Fig. 3a). This feature of an increased baroclinity around 60 °N is also evident in the composite difference between SICnotrd- and SICnotrd+ years based on the detrended ERA5 reanalysis data (Fig. 3b) that is well captured by the model sensitivity experiments (Fig. 3c) through atmospheric dynamics-driven processes rather than from physical processes associated with diabatic heating or vertical diffusion, etc. (Supplementary Fig. 7). The warming magnitudes in the detrended data and model simulations are weaker than the strong warming effect in the original data because the long-term global warming trend has been removed in the detrended data; moreover, the SST distributions outside the perturbed Arctic region in the model simulations are identical and the climate forcing agents such as greenhouse gases (GHGs) and aerosols repeat the same climatological cycle each year in both SICexp- and SICexp+ experiments so as to isolate the modeled response to regional Arctic sea-ice reduction

and local SST warming. Nevertheless, the meridional temperature structures showing similar temperature gradient patterns correspond to similar circulation changes in zonally-averaged zonal wind through the thermal wind relation, manifesting a poleward shift of the subtropical jet stream and storm tracks in all three reanalysis- and model-based analyses (Fig. 3d-f). These poleward shifts are also evident in horizontal wind and precipitation fields, which result in a wetter Pacific coast and most inland regions in Alaska and Canada but a drier western and midwestern U.S. (Fig. 3g-i). These changed hydroclimate conditions between SIC- and SIC+ years are consistent across different observational and reanalysis precipitation datasets (Supplementary Fig. 8) other than the one used here. The associated anticyclonic circulation anomaly over the western U.S. also suppresses cloud formation with enhanced downward motion and incoming solar radiation, resulting in hotter and drier surface weather that is synergistically favorable for enhanced fuel aridity in fire-prone regions (Fig. 3j-l). The consistency between the original and detrended reanalysis data suggests a robust dynamical linkage between the Arctic sea ice and regional fire weather on both long-term and short-term time scales, while the resemblance between the modeling results and the reanalysis-based results confirms the significant impact of Arctic sea-ice loss on regional fire weather deterioration through modulating regional circulations with poleward shifted North Pacific jet stream and worsened fire-favorable surface weather conditions over the western U.S.

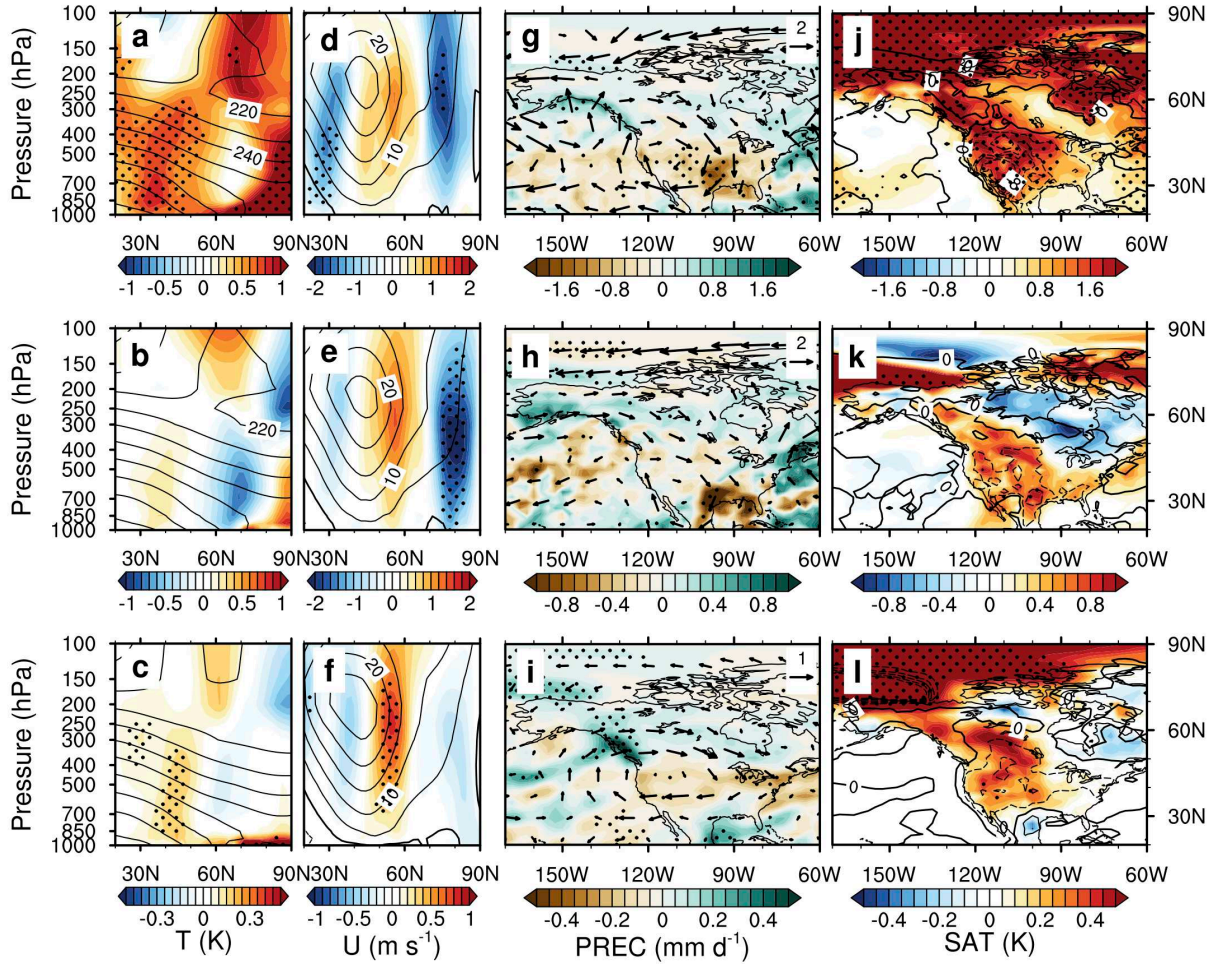


Fig. 3. Physical processes underlying the Arctic sea ice and fire teleconnection. **a**, zonally-averaged (170 °W to 60 °W; as shown in **g**) temperature difference (shading) in autumn and early winter (September to December) between the SIC- and SIC+ years based on the original ERA5 reanalysis data. The time average of zonally-averaged temperature in the SIC+ years is also shown (contours; unit: K). **b**, As in **a**, but for the difference between the SICnotrd- and SICnotrd+ years based on the detrended ERA5 reanalysis data. **c**, As in **a**, but for the difference between the SICexp- and SICexp+ experiments based on the CESM-RESFire simulations. **d-f**, As in **a-c**, but for zonally-averaged zonal wind based on the original ERA5 reanalysis data, the detrended ERA5 reanalysis data, and the CESM-RESFire simulations, respectively. **g-i**, As in **a-c**, but for wind circulation at 500 hPa (arrows; unit: m s^{-1}) and total precipitation rate (shading) differences based on the original ERA5 reanalysis data, the detrended ERA5 reanalysis data, and the CESM-RESFire simulations, respectively. **j-l**, As in **a-c**, but for 2-m relative humidity (contours with negative values in dashed lines; unit: %) and 2-m air temperature (shading) differences based on the original ERA5 reanalysis data, the detrended ERA5 reanalysis data, and the CESM-RESFire simulations,

respectively. Stipples in **a-l** show regions that are significantly different from 0 at the 0.1 significance level of two-sided t-test.

The synergistic effects of these multivariate fire weather changes following pre-conditioned peak fire season during climatologically hot and dry summer prolongs regional fire season and exacerbates burning severity in the subsequent autumn and early winter following diminished Arctic sea ice, making the prediction of fire hazards well-suited to an analysis of compound climate extreme events³¹. However, the complexity of the multiple interactive pathways and processes in climate systems also increases the difficulty of detection and attribution of climate extreme events in the observed historical records. As mentioned above, the model simulated warming and associated hydroclimate anomalies are generally weaker than the reanalysis-based composite difference because of the fixed climate forcing agents such as GHGs and extra-polar SST changes other than the Arctic sea-ice loss induced warming effect in the modeling sensitivity experiments. The missing global warming effect in the atmosphere and extra-polar oceans in the model limits its capability to answer the second question about the relative importance of the Arctic-driven teleconnection effect in the observed total fire weather changes associated with all climate forcing and processes. To improve the robustness of our analysis and preclude the potential influence of other processes and pathways driven by variable climate forcing agents (e.g., increasing GHGs in the past four decades) on historical regional fire weather changes, we also examine the difference of climate responses between the Atmospheric Model Intercomparison Project (amip)³² and its counterfactual counterpart with pre-industrial forcing (amip-piForcing or AMIP SSTs with control forcing)³³ experiments in the latest Coupled Model Intercomparison Project Phase 6 (CMIP6) (see Methods). These two experiments share the same realistic and observationally-based SST and sea-ice surface conditions from 1979 to near

present-day but expose model sensitivity to different anthropogenic forcing levels of GHGs, aerosols, and land use change by simulating the model response to time varying realistic forcing levels (as in the amip scenario) and to forcing levels held constant at pre-industrial levels (as in the amip-piForcing scenario). The differences between the SIC- and SIC+ years in both amip (Supplementary Fig. 9a-d) and amip-piForcing (Supplementary Fig. 9e-h) experiments agree with each other with minor changes in fire-related climate responses, suggesting a dominant role of ocean/sea-ice surface conditions in driving the observed fire weather changes (i.e., fire weather changes over the U.S. resembles each other in the amip and amip-piForcing experiments despite different levels of atmospheric and terrestrial forcing agents). The difference between these two experiments further reveals almost opposite climate effects of anthropogenic and natural forcing through atmospheric and land processes on regional fire weather changes. Specifically, only the response in warmer surface air temperature (Supplementary Fig. 9l) over the continental U.S. is consistent with the reanalysis-based composite result (Fig. 3j), while the climate responses to the airborne and terrestrial anthropogenic forcing (i.e., GHGs, aerosols, and land use change) reflected in zonally-averaged temperature (Supplementary Fig. 9i) and wind (Supplementary Fig. 9j) fields as well as horizontal wind circulation and precipitation (Supplementary Fig. 9k) show distinct signatures that differ from the reanalysis-based results (Fig. 3a/d/g). These results indicate that the observed regional fire weather changes between the SIC- and SIC+ years are strongly controlled by oceanic surface conditions including both sea-ice and SST changes in a warming climate rather than by a direct response through atmospheric or terrestrial processes to the climate forcing agents. The SST and sea-ice changes appear to be the critical ingredients in eliciting the regional fire weather conditions conducive to more large wildfires—but which one is more important? We further conduct a pattern recognition method

known as the “signal-to-noise-maximizing pattern (S/NP) filtering method”³⁴ based on the ERA5 reanalysis and the amip model ensemble to separate forced responses in regional fire weather due to other climate variability such as tropical ocean variations associated with ENSO (see Methods). The multi-field pattern filtering results show ENSO- and Arctic-driven hemispherical teleconnection patterns emerging in the first (S/NP1; Supplementary Fig. 10) and third (S/NP3; Supplementary Fig. 11) groups of S/NPs, respectively. These two groups of S/NPs also show constructive contributions by variations in tropical and Arctic surface conditions to regional fire weather changes, both of which result in a warmer and drier western U.S. during the SIC- years by similar magnitudes. Repeating this analysis using the detrended ERA5 reanalysis and amip-Forcing data shows similar results (e.g., a hotter and drier western U.S. during the SICnotrd-years) that are also constructively contributed by interannual variations of both ENSO (Supplementary Fig. 12) and Arctic sea ice (Supplementary Fig. 13) even when the long-term global warming and AA effects have been removed in the detrended data. Therefore, these climate diagnostic results along with our Arctic sea ice sensitivity experiments support the hypothesis that Arctic surface conditions play an important and synergistic role in determining regional fire weather and burning activity changes over the western U.S. across interannual to interdecadal scales. Given the continuously increasing trend in the S/NP3 time series and decreasing trend in Arctic sea ice (Supplementary Fig. 11), Arctic-driven teleconnection effects are expected to play an increasingly prominent role in modulating regional fire weather in the future.

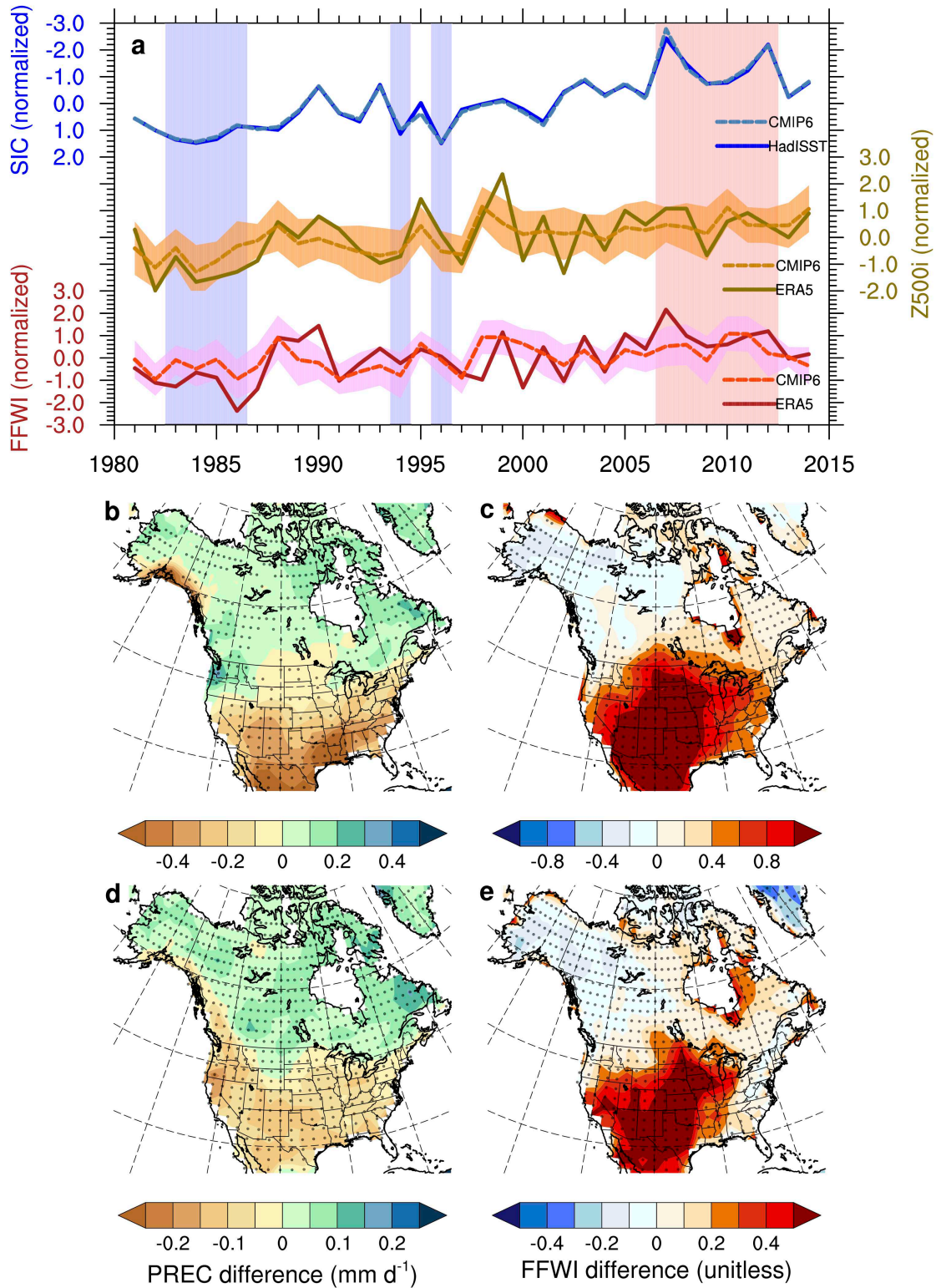


Fig. 4. Arctic sea ice and regional fire weather teleconnection in the CMIP6 amip experiment. **a**, time series of normalized SIC, Z500i, and FFWI based on the observational/reanalysis data and 15 CMIP6 model ensemble. The

shading along lines of the time series denotes ± 1 standard deviations of the model ensemble, and the vertical bar shading denotes years with minimum (pink; SIC-) and maximum (blue; SIC+) SIC for the composites in **b** and **c**. **b**, total changes in precipitation rates in autumn and early winter (September to December) between the SIC- and SIC+ years based on the 12 CMIP6 model ensemble. **c**, As in **b**, but for total changes in FFWI. **d**, the Arctic-driven (S/NP3) changes in precipitation rates in autumn and early winter (September to December) between the SIC- and SIC+ years based on the 12 CMIP6 model ensemble. **e**, As in **d**, but for the Arctic-driven (S/NP3) changes in FFWI based on the 12 CMIP6 model ensemble. Stipples in **b-e** show regions that 2/3 CMIP6 models agree on the signs.

The hypothesized Arctic-driven teleconnection has been further examined using the amip simulations to corroborate the robustness of these relationships across different CMIP6 participating models. Since the amip experiment uses the observational SST and sea ice surface boundary conditions, the time series of SIC in the CMIP6 model ensemble is almost identical to the observational data (Fig. 4a). The ensemble simulated atmospheric and land surface fire weather variations in terms of Z500i ($r_{\text{CMIP6-ERA5}}^{\text{Z500i}} = 0.74$; p value < 0.01) and FFWI ($r_{\text{CMIP6-ERA5}}^{\text{FFWI}} = 0.54$; p value < 0.01) also reproduce the reanalysis-based inter-annual and inter-decadal variations in general, with comparable correlation coefficients among SIC, Z500i, and FFWI between the CMIP6 model ensemble and the reanalysis data (Supplementary Fig. 14). All 15 models capture the correct signs of correlations between SIC and Z500i as well as Z500i and FFWI, respectively, and a majority of participating models (12 out of 15) successfully reproduce the negative correlation between SIC and FFWI with 5 of them showing statistically significant negative correlations like that found in the reanalysis data (Supplementary Fig. 14). We then analyze the spatial distributions in the 12 CMIP6 models showing correct SIC-FFWI correlations by comparing the differences of non-filtered (Fig. 4b, c) and S/NP3 filtered patterns (Fig. 4d, e) in precipitation and FFWI between the SIC- and SIC+ years to tease out the role of the Arctic-driven fire weather changes in all forcing-driven changes. The changes in S/NP3 filtered fields

appear to be mostly driven by the Arctic change, with little forced response evident from other climate drivers. Though the magnitudes of the Arctic-driven precipitation (Fig. 4d) and fire weather changes (Fig. 4e) are about half of the corresponding total changes (Fig. 4b, c), the north-south contrast spatial patterns are well preserved in the S/NP3 filtered fields with severely deteriorated fire weather occurring over the western U.S. during SIC- years. The lower ranking and larger ensemble spread of S/NP3 (Supplementary Fig. 11) than S/NP1 (Supplementary Fig. 10) suggest a lower signal-to-noise ratio of Arctic-driven teleconnection effects than ENSO-driven effects in the CMIP6 models, which is partly responsible for the controversial role of high-latitude changes in middle-latitude climate and weather extremes owing to diversified climate modeling responses to Arctic sea-ice loss^{23,35}. Improvement on the representation of Arctic-midlatitude teleconnection in ESMs might pose another grand challenge to climate model development because of all the complex dynamic and physical processes involved in the long teleconnection pathway across different components of the Earth system.

Recently, considerable progress has been made to understand the linkage between high-latitude climate change and midlatitude weather extremes, but there is a lack of consensus among the community about the potential mechanisms due to the relatively short length of observational datasets and low signal-to-noise ratios in climate modeling results²³. Most previous studies have focused on the Arctic influence on climate and weather extremes in summer or winter²³, with transitional seasons such as spring and autumn receiving less attention. The competition of different dynamic pathways and processes³⁶ in those transitional seasons increases the difficulty of obtaining a clear view (with consensus) about the climate influence on compound extreme events such as the fire hazard discussed here. Our combined analyses based on both single forcing-oriented climate sensitivity experiments and all forcing-included ensemble historical

modeling experiments enable us to understand the physical mechanism underlying the statistical relationship as well as its relative contributions to the observed total changes. Although some interactive processes such as ocean-atmosphere coupling and fire-climate feedbacks are still missing in the modeling experiments used in this study, previous studies have investigated the possible influence of those interactive processes and suggested consistent but amplified climate responses through ocean-atmosphere coupling³⁷ and nonnegligible but secondary fire-climate feedbacks through land-atmosphere coupling³⁸. Moreover, more coordinated climate modeling intercomparison projects such as the Polar Amplification Model Intercomparison Project (PAMIP)³⁹ and the Fire Model Intercomparison Project (FireMIP)⁴⁰ have been proposed and advanced, which could narrow down the knowledge gaps regarding the high-latitude and mid-latitude teleconnection and its role in increasing fire hazards.

More extreme fire weather with increasing likelihood of large wildfires in autumn has become the “new normal” for western coastal regions like California, a region projected to suffer more by the end of this century⁴¹. Previous studies have identified strategies for coexistence with wildfires in a changing world with escalating fire danger^{42,43}. But Arctic sea ice has been projected to continuously decline and eventually diminish to a sea ice-free Arctic in autumn by the 2050s⁴⁴, so more drastic changes might be anticipated. This study describes a mechanism indicating how the teleconnection between decreasing Arctic sea ice and worsening regional fire weather may sustain and even strengthen over the next few decades, favoring more and larger wildfires across the western U.S. and making this region even more vulnerable to destructive fire hazards. These implications may serve as motivation for more attention to adaptive resilience approaches including public awareness of fire risk and hazard mitigation, scientific forest and

fire risk management, and sustainable residential and infrastructure development planning on fire-prone landscapes^{42,43}.

Methods

Observation and reanalysis data

The $1^\circ \times 1^\circ$ gridded sea-ice concentrations at monthly frequency for 1981-2019 are provided by the Hadley Centre Sea Ice and Sea Surface Temperature dataset (HadISST)⁴⁵. Daily and monthly meteorological variables including air temperature, 2-m relative humidity, wind speed and vectors, total precipitation rates, and geopotential heights used for the FFWI calculation and fire weather composite analysis are collected and processed based on the ERA5 reanalysis dataset³⁰. We also analyzed the NASA's Modern-Era Retrospective Analysis for Research and Applications (MERRA-2)⁴⁶ reanalysis-based Canadian Forest Fire Weather Index (FWI)⁴⁷ from the Global Fire Weather Database (GFWED)⁴⁸ as well as multiple observation- and reanalysis-based precipitation datasets from the Global Precipitation Climatology Project (GPCP v2.3)⁴⁹, MERRA-2⁴⁶, Climate Forecast System Reanalysis (CFSR)⁵⁰, ERA-Interim⁵¹, and the Japanese 55-year Reanalysis (JRA-55)⁵² for testing the robustness of the Arctic sea ice-fire teleconnection in Supplementary Fig. 2 and Supplementary Fig. 8, respectively.

Burned areas of large wildfires (≥ 1000 acres) across the western U.S. from 1984 to the present are produced by the U.S. Geological Survey Center and the USDA Forest Service through the Monitoring Trends in Burned Severity (MTBS) program⁵³. The fractional changes of regional total burned area (BAC) in Fig. 1C, Supplementary Fig. 1c, and Supplementary Fig. 2c are given by:

$$BAC = \frac{\overline{BA}_{SIC-} - \overline{BA}_{SIC+}}{\frac{1}{2}(|\overline{BA}_{SIC-}| + |\overline{BA}_{SIC+}|)} ,$$

where \overline{BA}_{SIC-} and \overline{BA}_{SIC+} are the monthly total burned area of large wildfires averaged over the SIC-/SICnotrd- and SIC+/SICnotrd+ years, respectively (as shown in Fig. 1b, Supplementary Fig. 1b, and Supplementary Fig. 2b). We choose the average of $|\overline{BA}_{SIC-}|$ and $|\overline{BA}_{SIC+}|$ rather than $|\overline{BA}_{SIC+}|$ alone as the denominator in case of zero $|\overline{BA}_{SIC+}|$ in some months such as December or negative burned area anomalous values after detrending in SICnotrd- and SICnotrd+ years. In these cases, BAC becomes 200% or -200% according to the above equation (e.g., Dec in Fig. 1c; May-Jun and Sep-Nov in Supplementary Fig. 1c).

Models and experiments

We use a process-based CESM-RESFire model¹⁹ for the Arctic sea ice climate sensitivity experiments. The RESFire model was developed and coupled with both the land the atmosphere components of the CESM version 1.2 modeling system⁵⁴ with improved region-specific fire weather and socioeconomic constraints and fire feedbacks to the climate and vegetation. The land component we use for the sensitivity experiments is the Community Land Model version 4.5 (CLM4.5)⁵⁵, while the atmosphere component we use is the high-top Whole Atmosphere Community Climate Model (WACCM)⁵⁶, which is a comprehensive atmospheric model with a well-resolved stratosphere by 70 vertical levels up to 140 km at a horizontal resolution of 1.9° (latitude) × 2.5° (longitude). We first conduct 40-year simulations as a control (CTRL) run with annually repeating prescribed climatological (1981–2010 average) SIC and SST from the HadISST dataset⁴⁵ to provide initial conditions. We then branch two climate sensitivity experiments (SICexp+ and SICexp-) from July to December of each modeling year by perturbing SIC and SST in the Pacific sector of the Arctic (120 °E to 135 °W; 70 °N to 80 °N; as shown in

Fig. 2a) from July to October to investigate the climate sensitivity to regional Arctic SIC and associated local SST changes. The selection of the perturbation months is based on the correlation coefficients of seasonal FFWI and monthly Arctic SIC of the same years that are statistically significant with both original and detrended monthly SIC time series. In the SICexp+ experiment, we replace the climatological SIC and SST in the selected Arctic region with the averaged SIC and SST over the six maximum SIC years (1983, 1984, 1985, 1986, 1994, 1996; as shown in Fig. 1b) above positive one standard deviation ($> +1\sigma$) of the normalized regional SIC during 1981-2019. In the SICexp- experiment, we replace the climatological SIC and SST in the selected Arctic region with the averaged SIC and SST over the six minimum SIC years (2007, 2008, 2012, 2016, 2017, 2019; as shown in Fig. 1b) below negative one standard deviation ($< -1\sigma$) of the normalized regional SIC during 1981-2019. All other conditions such as the initial conditions, extra-polar SST boundary conditions, as well as lightning and population density for natural and anthropogenic fire ignition are kept the same in both experiments (Supplementary Table 1). This method has been applied in similar sea ice-focused climate sensitivity studies^{57,58}. To focus only on the climate effects on fire, we turn off the fire feedback processes including online coupled fire emissions and fire-induced land cover change in the RESFire model. These feedback processes would exert nonnegligible but secondary effects by either amplifying or damping regional climate-fire sensitivity relations as suggested by our previous study³⁸.

Besides the CESM-RESFire climate sensitivity experiments, we also examine the Arctic sea ice-fire teleconnection in multiple CMIP6 climate modeling systems participating in the amip³² and amip-piForcing³³ experiments. There are 15 CMIP6 models (Supplementary Table 2) in total that provide the daily and monthly model outputs of the amip experiment for the FFWI calculation and fire weather analysis in Fig. 4, while 4 CMIP6 models (Supplementary Table 3) provide the

monthly model outputs of the amip-piForcing experiment for the fire weather composite analyses in Supplementary Figs. 9, 12, and 13. Most model outputs in both amip and amip-piForcing experiments end in 2014, so the composite years for the SIC- group (2007 to 2012; as shown in Fig. 4a and Supplementary Figs. 10c/11c) in these CMIP6 models are slightly different from those in the ERA5-based composite analysis (the composite years for the SIC+ group are the same as shown in Fig. 4a). For the S/NP filtering analyses based on detrended amip-piForcing data, all the composite years for both SICnotrd- (1981, 1990, 1993, 2007, 2008, 2012; as shown in Supplementary Figs. 12c/13c) and SICnotrd+ (1994, 1996, 2000, 2001, 2013; as shown in Supplementary Figs. 12c/13c) groups are also slightly different from those in the ERA5-based SICnotrd- (with one more year of 2019) and SICnotrd+ (with one more year of 2018) groups in Supplementary Fig. 1.

Climate and weather indices

FFWI²⁹ is an empirical fire weather index derived from a part of the National Fire Danger Rating System (NFDRS)⁵⁹ for measuring the weather influence on fire danger in the U.S. It is calculated based on surface air temperature, 2-m relative humidity, and surface wind speed with larger values implying higher fire potential. FFWI is given by:

$$FFWI = \frac{\eta\sqrt{1+U^2}}{0.3002},$$

where U is surface wind speed in miles per hour and η is the moisture damping coefficient.

$$\eta = 1 - 2\left(\frac{EMC}{30}\right) + 1.5\left(\frac{EMC}{30}\right)^2 - 0.5\left(\frac{EMC}{30}\right)^3,$$

where EMC is the equilibrium moisture content as a function of surface air temperature T in degrees Fahrenheit and relative humidity RH in percentage:

$EMC =$

$$\left\{ \begin{array}{l} 0.03229 + 0.281073 \times RH - 0.000578 \times T \times RH, \text{ for } RH < 10\% \\ 2.22749 + 0.160107 \times RH - 0.01478 \times T, \text{ for } 10\% < RH \leq 50\% \\ 21.0606 + 0.005565 \times RH^2 - 0.00035 \times T \times RH - 0.483199 \times RH, \text{ for } RH > 50\% \end{array} \right. .$$

This index is a simplified form of the burning index (BI) in NFDRS that only requires meteorological values at observational time or corresponding modeling outputs. It has been previously used for weekly to seasonal fire danger forecasts and validations not only for the U.S. but also for other global regions⁶⁰. In comparison, the MERRA-2-based FWI⁴⁷ is a more sophisticated system based on multiple fuel moisture codes and fire behavior indices, which are derived from meteorological variables including surface air temperature, relative humidity, wind, and precipitation. We chose FFWI in combination with precipitation rather than FWI for fire weather analysis in the main text because of its ease of use and weather/fuel data availability from climate model outputs.

We calculate the gridded FFWI based on the daily ERA5 reanalysis data and climate modeling outputs from CESM-RESFire and CMIP6 models. The regional average FFWI, NFIRE, and FIREsize for the correlation and composite analysis in Figs. 1, 2 and 4 are estimated using grid-area weighted average over the western U.S. (as shown in Fig. 1a and Fig. 2a). Similarly, the regional average SIC time series in Fig. 1b, Fig. 4a, and Supplementary Fig. 2b without detrending and the SIC time series in Supplementary Fig. 1b after detrending are estimated using the same method over the Pacific sector of the Arctic (as shown in Fig. 1a and Fig. 2a). Z500i is estimated by projecting the anomalous geopotential height at 500 hPa in either the reanalysis

data or the modeling results onto an identified fire-favorable circulation pattern over the northeastern Pacific and western U.S. (135 °W to 90 °W; 25 °N to 55 °N; as shown in Supplementary Fig. 2a), which is obtained by regressing the ERA5-based anomalous geopotential height at 500 hPa onto the seasonal and regional average FFWI time series over the western U.S. After regional averaging or summation, the time series in Fig. 1b (SIC only), Fig. 4a, Supplementary Fig. 1b, and Supplementary Fig. 2b are also normalized for direct comparison against each other before the composite and correlation analysis. The univariate (1-D) and bivariate (2-D) distribution densities for each index in Fig. 2b-e are then generated and visualized using the Seaborn Python library⁶¹ based on the Kernel Density Estimation (KDE) method.

The bi-monthly Multivariate El Niño-Southern Oscillation index (MEI)⁶² is the time series of the leading combined Empirical Orthogonal Function (EOF) of five different variables (sea level pressure, SST, zonal and meridional components of the surface wind, and outgoing longwave radiation) over the tropical Pacific basin (30°S to 30°N; 100°E to 70°W). We use MEI for comparing and interpreting the identified S/NP forced responses. The S/NP1 timeseries in both original and detrended data show strong correlations with MEI ($r=0.96$ with p value <0.01 in Supplementary Fig. 10; $r=0.93$ with p value <0.01 in Supplementary Fig. 12), suggesting this pattern as the most prominent climatic signal is closely related to the coupled ocean-atmosphere conditions in the tropical Pacific.

Statistical analysis and significance tests

We first conduct composite analyses based on original or detrended observational and reanalysis data to identify regional fire weather responses to the Arctic sea ice changes on both interdecadal

to interannual time scales. The members in each composite group are selected based on the regional averaged and normalized SIC time series before (Fig. 1b) and after detrending (Supplementary Fig. 1b). We use ± 1 standard deviations of the original (detrended) SIC time series as thresholds for selecting members in SIC-/SIC+ (SICnotrd-/SICnotrd+) groups in Fig. 1 (Supplementary Fig. 1). Please note that the MTBS burned area in Supplementary Fig. 1c and meteorological variables such as Z500 and FFWI in Supplementary Fig. 1a/b and air temperature, zonal winds, precipitation, and relative humidity in Fig. 3b/e/h/k are also detrended to keep consistent with the detrended SIC time series in SICnotrd-/SICnotrd+ groups. The long-term trends in time series are removed using the NCL *dtrend* function, while the trends in gridded data are removed by first estimating long-term trends in zonal mean values and then subtracting these trends from gridded values at same latitudes to retain heterogeneity in the zonal direction after removing global warming effects and their footprint in the meridional direction such as AA. In this way, the strong global warming effect is largely removed in the detrended data as shown in Fig. 3b/k.

We then use a two-sided Student's t-test to test the statistical significance of the differences between two groups of time averaged data such as the seasonal/monthly FFWI composites in Fig. 1a/c ($n=6$), model simulated seasonal burned area composites in Fig. 2a ($n=40$), and seasonal fire weather variables in Fig. 3 ($n=6$ for reanalysis-based data and $n=40$ for model-based data). These data generally satisfy the assumptions of the t-test including normality and randomness of samples. If a p value obtained from the t-test is no larger than a threshold, e.g., $\alpha = 0.01, 0.05, \text{ or } 0.1$, then we reject the null hypothesis of equal averages in the sample groups at certain significance levels corresponding to the threshold. We also use a stricter control of False Discovery Rate (FDR) method⁶³ to protecting against overstatement of multiple-testing

results due to the influence of possible spatial correlation in Fig. 1a and Fig. 2a. Local null hypotheses of each grid cell are rejected if their respective p values are no larger than a threshold level p_{FDR}^* that depends on the distribution of the sorted p values:

$$p_{FDR}^* = \max_{i=1, \dots, N} [p_{(i)}; p_{(i)} \leq (i/N)\alpha_{FDR}],$$

where N is the number of testing grid cells and α_{FDR} is the chosen control level for the FDR method. For data grids exhibiting moderate to strong spatial correlation, we can achieve approximately correct global test levels by choosing $\alpha_{FDR} = 2\alpha_{global}$ for the FDR method⁶³. For the modeling results from different CMIP6 climate modeling systems in Fig. 4 and Supplementary Fig. 9, we compare their consistency in simulated fire weather responses to test the robustness of the climate-fire teleconnection across those models.

To estimate the uncertainty of the probability and intensity changes of extreme burning years, we use a bootstrap method by resampling the model-simulated samples with or without replacement for 10000 times ($n=10000$) and then repeatedly estimating the statistics such as the probability and intensity of extreme years based on the resampled data from each experiment (see Supplementary Figs. 5/6). By analyzing the newly generated samples from the bootstrap method, we can obtain the statistics of the variables of interest such as the 95% inter-percentile ranges (i.e., percentile values between 2.5% and 97.5%) of the probability of extreme members. These extreme members are defined as modeling years with regional total burned area values above the 95% percentile in the samples of the SICexp+ experiment. Therefore, the probability of extreme years in the SICexp+ experiment ($P_{SICexp+}^{extreme}$) is always 5% in the SICexp+ bootstrap resampling data by definition, while the probability of extreme years in the SICexp- experiments ($P_{SICexp-}^{extreme}$) varies due to the mutable resampled data subsets (except the unique subset with the sample size

of all 40 modeling years in the non-replacement case). We also test the robustness of these statistical estimates against different ensemble sizes in Supplementary Fig. 6, which shows the probabilities of extreme burning years converging with increasing ensemble sizes of the bootstrap resampling groups. The 40-year ensemble size is large enough to separate the probability of extreme years in the SICexp- experiment ($P_{SICexp-}^{extreme} = 20\%$ with the 95% inter-percentile range of [6.6%, 38.9%]) from that in the SICexp+ experiment (i.e., $P_{SICexp+}^{extreme} = 5\%$ is outside of the 95% inter-percentile range of $P_{SICexp-}^{extreme}$) even with replacement in the bootstrap resampling processes. This method has been applied in our previous climate extreme modeling study⁵⁸ and other similar applications⁶⁴.

The signal-to-noise-maximizing pattern filtering method³⁴ has been used to separate forced climate responses from each other as well as from climate internal variability. The S/NP filtering method relies on a pattern recognition method named linear discriminant analysis to identify spatial patterns as linear combinations of EOFs that maximize the variance of signal-to-noise ratios among an ensemble of realizations³⁴. Here “signal” is defined by the mean over the ensemble, which consists of the ERA5 reanalysis data and the amip (as listed in Supplementary Table 2 except CESM2, CESM2-WACCM, and IPSL-CM6A-LR that fail to capture the correct correlations between SIC and FFWI as shown in Supplementary Fig. 14) or amip-piForcing (as listed in Supplementary Table 3) models. The ranking of identified S/NP patterns denotes the intensity of the corresponding signal in the ensemble (i.e., signal intensity from high to low with increasing ranking). Therefore, the S/NP ranking results are slightly affected by the ensemble composition given different signal-to-noise ratios in each amip or amip-piForcing model, while the spatial distributions and temporal variations of each S/NP are less sensitive to the ensemble composition. Another advantage of this S/NP filtering method over the simple ensemble

averaging method is that it greatly reduces the number of ensemble members needed to estimate forced responses by a factor of 7~10 compared to simple ensemble averaging³⁴. As suggested by Wills et al.³⁴, the S/NP-filtered estimate of forced responses based on 3 ensemble members is better than the simple ensemble average of 20 members, and the S/NP-filtered estimate based on 2 ensemble members is only slightly worse. This improved signal-to-noise detection efficiency is of great help for our analyses here given limited numbers of CMIP6 models that provide necessary modeling outputs for the ensemble. We apply this S/NP filtering method to a multi-variable anomaly field based on seasonal mean surface air temperature, precipitation, FFWI, and Z500 in the Northern Hemisphere from each model. Such combined analysis on all four meteorological fields improves the identification capability and robustness of climate responses to different forcing such as ENSO and AA. After pattern recognition, we calculate the correlation coefficients between timeseries (1981-2014) of these identified S/NPs and climate indices of interest (MEI and SIC in this application) to infer their driving forces. In the S/NP filtering analysis based on the original ERA5 reanalysis and amip modeling data, S/NP1 and S/NP3 show good correlations with MEI ($r=0.96$; p value <0.01 ; Supplementary Fig. 10) and SIC ($r=-0.75$; p value <0.01 ; Supplementary Fig. 11), respectively, implying different climate drivers and teleconnection pathways in these two S/NPs. Similarly, S/NP1 and S/NP8 show relatively lower and but still significant correlations with detrended MEI ($r=0.93$; p value <0.01 ; Supplementary Fig. 12) and detrended SIC ($r=-0.29$; p value $=0.09$; Supplementary Fig. 13) in the S/NP filtering analysis based on the detrended ERA5 reanalysis and amip-piForcing data. We then do the composite analysis for each S/NP by comparing differences between the SIC- (SICnotrd-) and SIC+ (SICnotrd+) years to identify forced responses to different climate drivers on multiple time scales. The S/NP composite results are shown in Fig. 4d/e in the main text as well as in

Supplementary Figs. 10-13. We test the robustness of those results by using different CMIP6 experiments (i.e., amip vs. amip-piForcing) or different subsets of the amip models in the ensemble. The MEI-related pattern stays in S/NP1 as the strongest signal across different CMIP6 models, while the ranking of the SIC-related pattern varies between the second and the third (e.g., the SIC-related pattern emerges in S/NP2 if using the 5 best-performed amip models (ACCESS-CM2, FGOALS-g3, GFDL-CM4, SAM0-UNICON, and UKESM1-0-LL showing significant negative correlations between SIC and FFWI in Supplementary Fig. 14), while it stays in S/NP3 if using all 15 amip models) in the amip ensemble and drops to the eighth in the detrended amip-piForcing ensemble. These results suggest a lower signal-to-noise ratio of the Arctic-driven climate effects (as shown in S/NP2 or S/NP3 based on amip data, or S/NP8 based on detrended amip-piForcing data) than that of the ENSO-driven ones (as shown in S/NP1) in CMIP6 models. However, this lower ranking does not necessarily imply that the Arctic-driven effects are weaker than ENSO-driven effects. The relative importance of different climate forcing factors should be inferred by the composite analysis for each S/NP, which suggests comparable impacts on regional fire weather by ENSO-driven (Supplementary Fig. 10 and Supplementary Fig. 12) and Arctic-driven (Supplementary Fig. 11 and Supplementary Fig. 13) teleconnection processes in both original and detrended data. For example, the magnitudes of the Arctic-driven changes in S/NP3 (Supplementary Fig. 11) based on the original data with both interannual and interdecadal variability are on the same level of the ENSO-driven changes in S/NP1 (Supplementary Fig. 10). Even when the global warming and Arctic amplification effects have been removed in the detrended ERA5 and amip-piForcing data, those S/NP patterns (S/NPs2-7) with higher rankings than the Arctic-driven one (S/NP8) show subtle differences between the SICnotrd- and SICnotrd+ years, making the Arctic-driven changes in S/NP8 as the

second largest contributor to fire-favorable weather conditions over the western U.S. on shorter (interannual) time scales (Supplementary Fig. 13). Moreover, the time series of Arctic-driven patterns in S/NP3 (Supplementary Fig. 11) show a much stronger increasing trend than others on interdecadal time scales, indicating an increasingly important role of the Arctic changes in modulating regional climate and fire weather over North America. Please refer to Wills et al.³⁴ for more technical details of the mathematical basis and climate research applications of this method.

Dynamic diagnosis

We examine daily temperature tendencies in CESM-RESFire modeling outputs to quantify the contributions from different dynamic and physical processes to the simulated climate responses in Fig. 3. The total temperature tendency (TTEND) consists of two components driven by dynamic processes (DTCORE) and physical processes (PTTEND). The latter can be further decomposed into four major physical processes: moisture processes (DTCOND), longwave heating (QRL), shortwave heating (QRS), and vertical diffusion (DTV). There is one more physical process related to gravity wave drag (TTGW), which is small and negligible in the troposphere of modeling outputs. Therefore, the contribution to the regional average meridional temperature gradient anomaly ($\Delta T = |T_{warm}| - |T_{cool}|$; as shown in Supplementary Fig. 7) from each process is given by:

$$\Delta T_{t_1} = \Delta T_{t_0} + \int_{t_0}^{t_1} TTEND dt,$$

where $TTEND = DTCORE + PTTEND = DTCORE + (DTCOND + QRL + QRS + DTV)$, and $\Delta T_{t_0} = 0$ at the beginning of the sea ice perturbation.

The sign and magnitude of ΔT depends on the competition of dynamic and physical processes at each timestep. The time evolution of ΔT shows that it stays above zero in general from September to November (Supplementary Fig. 7), which coincides well with the timing of strong positive fire anomalies (Supplementary Fig. 4).

Besides, note that the meridional temperature gradients remain positive in both the amip and amip-piForcing model ensembles (Supplementary Fig. 9a/e), while the sign and pattern reverse in the difference between these two experiments (Supplementary Fig. 9i). Such results imply that atmospheric and land processes induced by natural and anthropogenic forcing (i.e., GHGs, aerosols, and LULCC) cannot explain the observed circulation and fire weather changes (e.g., Fig. 3a-d) between the SIC- and SIC+ years. Please refer to the main text for detailed analysis and interpretation.

Acknowledgments: This research used resources of NERSC, a U.S. Department of Energy Office of Science User Facility operated under Contract No. DE-AC02-05CH11231. We thank DOE's RGMA program area, the Data Management program, and NERSC for computational resources to simulate climate sensitivity experiments and to analyze the CMIP6 data. We thank the World Climate Research Programme (which coordinated and promoted CMIP6 through its Working Group on Coupled Modeling), and each contributing climate modeling group for producing and making available their model output. We thank the Earth System Grid Federation (ESGF) for archiving the data and providing access and the multiple funding agencies who support CMIP6 and ESGF. We thank Robert Wills for sharing the code for the S/NP filtering analysis. We thank Jian Lu for helpful discussion to improve the dynamic analysis.

Funding: This research has been supported by the HiLAT-RASM project through the U.S. Department of Energy (DOE) Office of Science Regional and Global Model Analysis (RGMA) Program. The Pacific Northwest National Laboratory (PNNL) is operated for DOE by Battelle Memorial Institute under contract DE-AC05-76RLO1830.

Author contributions: Y.Z. conceived the research and designed climate sensitivity modeling experiments with P.J.R. and H.W. Y.Z. conducted the modeling experiments, processed the CMIP6 data, and prepared the first draft of the manuscript. All authors discussed the results and contributed to the writing of the manuscript.

Competing interests: Authors declare no competing interests.

Data and materials availability: The ERA5 reanalysis data are distributed by ECMWF from their web site at <https://www.ecmwf.int/en/forecasts/datasets/reanalysis-datasets/era5>. The gridded Arctic SIC and SST data are available at <https://www.metoffice.gov.uk/hadobs/hadisst/>.

The bi-monthly MEI.v2 is collected from the Physical Sciences Laboratory of National Oceanic and Atmospheric Administration (NOAA) at <https://psl.noaa.gov/enso/mei/>. The MTBS burned area data are available at <https://www.mtbs.gov/>. The MERRA-2-based FWI is distributed from the NASA Center for Climate Simulation Data portal at <https://portal.nccs.nasa.gov/datashare/GlobalFWI/>. The CMIP6 model outputs are distributed by the Earth System Grid Federation (ESGF) at <https://esgf-node.llnl.gov/search/cmip6/> (see Supplementary tables 2-3 for model details and references). The code for the S/NP filtering analysis is provided by Robert Wills at <https://github.com/rcjwills/forced-patterns>. All the CESM-RESFire modeling input and output data are archived on the GLADE and HPSS file systems managed by the National Energy Research Scientific Computing Center (NERSC). The simulation results of the CESM-RESFire sensitivity experiments used for the analysis in the main text have been deposited at the Figshare website (<https://figshare.com/s/4812b836025300f97183>) for the evaluation purpose. The modeling data and source code will also be made available to the public at <https://figshare.com/s/4812b836025300f97183> or other suggested data repositories upon publication.

References:

- 1 Radeloff, V. C. *et al.* Rapid growth of the US wildland-urban interface raises wildfire risk. *P Natl Acad Sci USA* **115**, 3314-3319 (2018).
- 2 Littell, J. S., McKenzie, D., Peterson, D. L. & Westerling, A. L. Climate and wildfire area burned in western U. S. ecoprovinces, 1916-2003. *Ecol Appl* **19**, 1003-1021, doi:Doi 10.1890/07-1183.1 (2009).
- 3 Dennison, P. E., Brewer, S. C., Arnold, J. D. & Moritz, M. A. Large wildfire trends in the western United States, 1984-2011. *Geophys Res Lett* **41**, 2928-2933, doi:10.1002/2014gl059576 (2014).
- 4 Fann, N. *et al.* The health impacts and economic value of wildland fire episodes in the US: 2008-2012. *Sci Total Environ* **610**, 802-809 (2018).
- 5 Thomas, D., Butry, D., Gilbert, S., Webb, D., and Fung, J. . The Costs and Losses of Wildfires: A Literature Survey (National Institute of Standards and Technology, 2017).
- 6 Syphard, A. D., Keeley, J. E., Pfaff, A. H. & Ferschweiler, K. Human presence diminishes the importance of climate in driving fire activity across the United States. *P Natl Acad Sci USA* **114**, 13750-13755, doi:10.1073/pnas.1713885114 (2017).
- 7 Balch, J. K. *et al.* Human-started wildfires expand the fire niche across the United States. *P Natl Acad Sci USA* **114**, 2946-2951 (2017).

- 8 Westerling, A. L., Hidalgo, H. G., Cayan, D. R. & Swetnam, T. W. Warming and earlier spring increase western US forest wildfire activity. *Science* **313**, 940-943, doi:10.1126/science.1128834 (2006).
- 9 Abatzoglou, J. T. & Williams, A. P. Impact of anthropogenic climate change on wildfire across western US forests. *P Natl Acad Sci USA* **113**, 11770-11775, doi:10.1073/pnas.1607171113 (2016).
- 10 Holden, Z. A. *et al.* Decreasing fire season precipitation increased recent western US forest wildfire activity. *P Natl Acad Sci USA* **115**, E8349-E8357 (2018).
- 11 Raymond, C. *et al.* Understanding and managing connected extreme events. *Nat Clim Change* **10**, 611-621 (2020).
- 12 Veraverbeke, S. *et al.* Lightning as a major driver of recent large fire years in North American boreal forests. *Nat Clim Change* **7**, 529-+, doi:10.1038/Nclimate3329 (2017).
- 13 Krawchuk, M. A. & Moritz, M. A. Constraints on global fire activity vary across a resource gradient. *Ecology* **92**, 121-132 (2011).
- 14 Marlon, J. R. *et al.* Long-term perspective on wildfires in the western USA. *P Natl Acad Sci USA* **109**, E535-E543, doi:10.1073/pnas.1112839109 (2012).
- 15 Aldersley, A., Murray, S. J. & Cornell, S. E. Global and regional analysis of climate and human drivers of wildfire. *Sci Total Environ* **409**, 3472-3481 (2011).
- 16 Jolly, W. M. *et al.* Climate-induced variations in global wildfire danger from 1979 to 2013. *Nat Commun* **6**, doi:ARTN 753710.1038/ncomms8537 (2015).

- 17 Shen, H. Z. *et al.* Global fire forecasts using both large-scale climate indices and local meteorological parameters. *Global Biogeochem Cy* **33**, 1129-1145 (2019).
- 18 Hantson, S. *et al.* The status and challenge of global fire modelling. *Biogeosciences* **13**, 3359-3375, doi:10.5194/bg-13-3359-2016 (2016).
- 19 Zou, Y. F. *et al.* Development of a REgion-Specific Ecosystem Feedback Fire (RESFire) Model in the Community Earth System Model. *J Adv Model Earth Sy* **11**, 417-445 (2019).
- 20 Screen, J. A. & Simmonds, I. The central role of diminishing sea ice in recent Arctic temperature amplification. *Nature* **464**, 1334-1337 (2010).
- 21 Cohen, J. *et al.* Recent Arctic amplification and extreme mid-latitude weather. *Nat Geosci* **7**, 627-637 (2014).
- 22 Coumou, D., Di Capua, G., Vavrus, S., Wang, L. & Wang, S. The influence of Arctic amplification on mid-latitude summer circulation. *Nat Commun* **9** (2018).
- 23 Cohen, J. *et al.* Divergent consensus on Arctic amplification influence on midlatitude severe winter weather. *Nat Clim Change* **10**, 20-29, doi:10.1038/s41558-019-0662-y (2020).
- 24 Strey, S. T., Chapman, W. L. & Walsh, J. E. The 2007 sea ice minimum: Impacts on the Northern Hemisphere atmosphere in late autumn and early winter. *J Geophys Res-Atmos* **115** (2010).

- 25 Deser, C., Tomas, R., Alexander, M. & Lawrence, D. The seasonal atmospheric response to projected Arctic sea ice loss in the late twenty-first century. *J Climate* **23**, 333-351 (2010).
- 26 Sewall, J. O. Precipitation shifts over western North America as a result of declining Arctic sea ice cover: The coupled system response. *Earth Interact* **9** (2005).
- 27 Cvijanovic, I. *et al.* Future loss of Arctic sea-ice cover could drive a substantial decrease in California's rainfall. *Nat Commun* **8** (2017).
- 28 Knapp, P. A. & Soule, P. T. Spatio-temporal linkages between declining Arctic sea-ice extent and increasing wildfire activity in the western United States. *Forests* **8** (2017).
- 29 Fosberg, M. A. Weather in wildland fire management: the fire weather index, in *Conference on Sierra Nevada Meteorology*. 4.
- 30 Copernicus Climate Change Service (C3S) (ed Copernicus Climate Change Service (C3S)) (Copernicus Climate Change Service Climate Data Store (CDS), 2017).
- 31 Zscheischler, J. *et al.* A typology of compound weather and climate events. *Nature Reviews Earth & Environment* **1**, 333-347, doi:10.1038/s43017-020-0060-z (2020).
- 32 Eyring, V. *et al.* Overview of the Coupled Model Intercomparison Project Phase 6 (CMIP6) experimental design and organization. *Geosci Model Dev* **9**, 1937-1958 (2016).
- 33 Webb, M. J. *et al.* The Cloud Feedback Model Intercomparison Project (CFMIP) contribution to CMIP6. *Geosci Model Dev* **10**, 359-384 (2017).

- 34 Wills, R. C. J., Battisti, D. S., Armour, K. C., Schneider, T. & Deser, C. Pattern Recognition Methods to Separate Forced Responses from Internal Variability in Climate Model Ensembles and Observations. *J Climate* **33**, 8693-8719, doi:10.1175/jcli-d-19-0855.1 (2020).
- 35 Screen, J. A. *et al.* Consistency and discrepancy in the atmospheric response to Arctic sea-ice loss across climate models. *Nat Geosci* **11**, 155-+ (2018).
- 36 Overland, J. E. *et al.* Nonlinear response of mid-latitude weather to the changing Arctic. *Nat Clim Change* **6**, 992-999, doi:10.1038/Nclimate3121 (2016).
- 37 Deser, C., Sun, L. T., Tomas, R. A. & Screen, J. Does ocean coupling matter for the northern extratropical response to projected Arctic sea ice loss? *Geophys Res Lett* **43**, 2149-2157 (2016).
- 38 Zou, Y. F. *et al.* Using CESM-RESFire to understand climate-fire-ecosystem interactions and the implications for decadal climate variability. *Atmos Chem Phys* **20**, 995-1020 (2020).
- 39 Smith, D. M. *et al.* The Polar Amplification Model Intercomparison Project (PAMIP) contribution to CMIP6: investigating the causes and consequences of polar amplification. *Geosci Model Dev* **12**, 1139-1164 (2019).
- 40 Rabin, S. S. *et al.* The Fire Modeling Intercomparison Project (FireMIP), phase 1: experimental and analytical protocols with detailed model descriptions. *Geosci Model Dev* **10**, 1175-1197 (2017).

- 41 Goss, M., Swain, D.L., Abatzoglou, J.T., Sarhadi, A., Kolden, C., Williams, A.P. and
Differbaugh, N.S. Climate change is increasing the risk of extreme autumn wildfire
conditions across California. *Environ Res Lett* **15**, 094016, doi:DOI: 10.1088/1748-
9326/ab83a7 (2020).
- 42 Moritz, M. A. *et al.* Learning to coexist with wildfire. *Nature* **515**, 58-66 (2014).
- 43 Schoennagel, T. *et al.* Adapt to more wildfire in western North American forests as
climate changes. *P Natl Acad Sci USA* **114**, 4582-4590, doi:10.1073/pnas.1617464114
(2017).
- 44 SIMIP Community. Arctic Sea Ice in CMIP6. *Geophys Res Lett* **47**, e2019GL086749,
doi:10.1029/2019gl086749 (2020).
- 45 Rayner, N. A. *et al.* Global analyses of sea surface temperature, sea ice, and night marine
air temperature since the late nineteenth century. *J Geophys Res-Atmos* **108** (2003).
- 46 Rienecker, M. M. *et al.* MERRA: NASA's Modern-Era Retrospective Analysis for
Research and Applications. *J Climate* **24**, 3624-3648 (2011).
- 47 Van Wagner, C. E. Development and Structure of the Canadian Forest Fire Weather
Index System. (Canadian Forest Service, Ottawa, Canada, 1987).
- 48 Field, R. D. *et al.* Development of a Global Fire Weather Database. *Nat Hazard Earth
Sys* **15**, 1407-1423 (2015).

- 49 Adler, R. F. *et al.* The Global Precipitation Climatology Project (GPCP) Monthly Analysis (New Version 2.3) and a Review of 2017 Global Precipitation. *Atmosphere-Basel* **9** (2018).
- 50 Saha, S. *et al.* The NCEP Climate Forecast System Version 2. *J Climate* **27**, 2185-2208 (2014).
- 51 Dee, D. P. *et al.* The ERA-Interim reanalysis: configuration and performance of the data assimilation system. *Q J Roy Meteor Soc* **137**, 553-597 (2011).
- 52 Kobayashi, S. *et al.* The JRA-55 Reanalysis: General Specifications and Basic Characteristics. *J Meteorol Soc Jpn* **93**, 5-48 (2015).
- 53 Jeff Eidenshink, B. S., Ken Brewer, Zhi-Liang Zhu, Brad Quayle, and Stephen Howard. A Project for monitoring trends in burn severity. *Fire Ecology Special Issue* **3**, 19 (2007).
- 54 Hurrell, J. W. *et al.* The Community Earth System Model A Framework for Collaborative Research. *B Am Meteorol Soc* **94**, 1339-1360 (2013).
- 55 Oleson, K. W., Lawrence, D. M., Bonan, G. B., Drewniak, B., Huang, M., Koven, C. D., Levis, S., Li, F., Riley, W. J., Subin, Z. M., Swenson, S. C., Thornton, P. E., Bozbiyik, A., Fisher, R., Heald, C. L., Kluzek, E., Lamarque, J.-F., Lawrence, P. J., Leung, L. R., Lipscomb, W., Muszala, S., Ricciuto, D. M., Sacks, W., Sun, Y., Tang, J., and Yang, Z.-L. Technical description of version 4.5 of the Community Land Model (CLM). 434 (National Center for Atmospheric Research, Boulder, CO, USA, 2013).

- 56 Marsh, D. R. *et al.* Climate Change from 1850 to 2005 Simulated in CESM1(WACCM). *J Climate* **26**, 7372-7391 (2013).
- 57 Screen, J. A., Simmonds, I., Deser, C. & Tomas, R. The Atmospheric Response to Three Decades of Observed Arctic Sea Ice Loss. *J Climate* **26**, 1230-1248 (2013).
- 58 Zou, Y. F., Wang, Y. H., Xie, Z. W., Wang, H. L. & Rasch, P. J. Atmospheric teleconnection processes linking winter air stagnation and haze extremes in China with regional Arctic sea ice decline. *Atmos Chem Phys* **20**, 4999-5017 (2020).
- 59 Jack D. Cohen, J. E. D. The National Fire-Danger Rating System: basic equations. Report No. General Technical Report PSW-82, 16 (P.O. Box 245, Berkeley, California 94701, 1985).
- 60 Roads, J., Fujioka, F., Chen, S. & Burgan, R. Seasonal fire danger forecasts for the USA. *Int J Wildland Fire* **14**, 1-18 (2005).
- 61 seaborn: statistical data visualization.
- 62 Wolter, K. & Timlin, M. S. Measuring the strength of ENSO events: How does 1997/98 rank? *Weather* **53**, 315-324, doi:10.1002/j.1477-8696.1998.tb06408.x (1998).
- 63 Wilks, D. S. "THE STIPPLING SHOWS STATISTICALLY SIGNIFICANT GRID POINTS" How Research Results are Routinely Overstated and Overinterpreted, and What to Do about It. *B Am Meteorol Soc* **97**, 2263-+ (2016).

- 64 Screen, J. A., Deser, C., Simmonds, I. & Tomas, R. Atmospheric impacts of Arctic sea-ice loss, 1979-2009: separating forced change from atmospheric internal variability. *Clim Dynam* **43**, 333-344 (2014).

Figure legends:

Fig. 5. Observation- and reanalysis-based Arctic sea ice and regional fire teleconnection. a, spatial distributions of the correlation (shading in the Arctic) between seasonal average Arctic sea-ice concentrations in summer and autumn (July to October) and seasonal and regional average FFWI over the western U.S. in the following autumn and early winter (September to December), and the difference of seasonal average FFWI (shading in the U.S.) between years with minimum (SIC-: red up-pointing triangles in **b**) and maximum (SIC+: blue down-pointing triangles in **b**) Arctic SIC. The difference of seasonal (September to December) average geopotential height at 500 hPa between the SIC- and SIC+ years is also shown (contours with negative values in dashed lines; unit: m). **b,** time series of seasonal and regional average SIC (seasonal mean from July to October; normalized by its 1981-2010 climatological mean and standard deviation), FFWI (seasonal mean from September to December), and their correlation. The region definitions for the Pacific sector of the Arctic and the western U.S. are outlined by red boxes in **a**. The horizontal dashed lines denote the ± 1 standard deviations of normalized SIC as thresholds for selecting the SIC \pm years. **c,** the composite of monthly FFWI (solid lines with dots and error bars) and fractional burned area change of large wildfires (vertical bars) over the western U.S. Error bars in **c** denote ± 1 standard deviations of monthly FFWI in each group. Stipples in **a** mark regions that are significantly different from 0 at the 0.05 significance level of two-sided t-test, and hatching in **a** denotes statistically significant regions based on the stricter FDR method (see Methods) with local gridded p value $\leq p_{FDR}^* = 0.0023$ at the threshold of $\alpha_{FDR} = 0.10$. Dot sizes for monthly FFWI in **c** denote the 0.05 (large) and 0.1 (medium) significance levels of two-sided t-test, respectively.

Fig. 2. CESM-RESFire simulated Arctic sea ice and regional fire teleconnection. **a**, spatial distributions of the seasonal average (July to October) sea-ice concentration difference (color shading in the Arctic Ocean) between the SICexp- and SICexp+ experiments, and the seasonal average (September to December) burned area change (color shading in North America) in response to the sea-ice perturbation. The difference of Z500 between SICexp- and SICexp+ is also shown (contours with negative values in dashed lines; unit: m). **b**, 2-dimensional distributions of the seasonal mean fire-favorable circulation index (Z500i; standardized by first removing the 40-year mean and then normalizing by the standard deviation of Z500i from the SICexp+ experiment) and FFWI (also standardized by the 40-year mean and standard deviation of FFWI from the SICexp+ experiment) based on the kernel density estimation (KDE) for SICexp- (red shading) and SICexp+ (blue contours). 1-d KDE distributions for each index in SICexp- (red) and SICexp+ (blue) are also shown along the x- and y-axis. **c**, As in **b**, but for the comparison of standardized FFWI and regional burned area (BA). **d**, As in **b**, but for the comparison of standardized FFWI and regional mean fire count (NFIRE). **e**, As in **b**, but for the comparison of standardized FFWI and regional mean fire size (FIREsize). Stipples in **a** show regions that are significantly different from 0 at the 0.1 significance level of two-sided t-test, and hatching in **a** denotes statistically significant regions based on the stricter FDR method (see Methods) with local gridded p value $\leq p_{FDR}^* = 0.017$ at the threshold of $\alpha_{FDR} = 0.20$.

Fig. 3. Physical processes underlying the Arctic sea ice and fire teleconnection. **a**, zonally-averaged (170 °W to 60 °W; as shown in **g**) temperature difference (shading) in autumn and early winter (September to December) between the SIC- and SIC+ years based on the original ERA5 reanalysis data. The time average of zonally-averaged temperature in the SIC+ years is also shown (contours; unit: K). **b**, As in **a**, but for the difference between the SICnotrd- and

SICnotrd+ years based on the detrended ERA5 reanalysis data. **c**, As in **a**, but for the difference between the SICexp- and SICexp+ experiments based on the CESM-RESFire simulations. **d-f**, As in **a-c**, but for zonally-averaged zonal wind based on the original ERA5 reanalysis data, the detrended ERA5 reanalysis data, and the CESM-RESFire simulations, respectively. **g-i**, As in **a-c**, but for wind circulation at 500 hPa (arrows; unit: m s^{-1}) and total precipitation rate (shading) differences based on the original ERA5 reanalysis data, the detrended ERA5 reanalysis data, and the CESM-RESFire simulations, respectively. **j-l**, As in **a-c**, but for 2-m relative humidity (contours with negative values in dashed lines; unit: %) and 2-m air temperature (shading) differences based on the original ERA5 reanalysis data, the detrended ERA5 reanalysis data, and the CESM-RESFire simulations, respectively. Stipples in **a-l** show regions that are significantly different from 0 at the 0.1 significance level of two-sided t-test.

Fig. 4. Arctic sea ice and regional fire weather teleconnection in the CMIP6 amip

experiment. a, time series of normalized SIC, Z500i, and FFWI based on the observational/reanalysis data and 15 CMIP6 model ensemble. The shading along lines of the time series denotes ± 1 standard deviations of the model ensemble, and the vertical bar shading denotes years with minimum (pink; SIC-) and maximum (blue; SIC+) SIC for the composites in **b** and **c**. **b**, total changes in precipitation rates in autumn and early winter (September to December) between the SIC- and SIC+ years based on the 12 CMIP6 model ensemble. **c**, As in **b**, but for total changes in FFWI. **d**, the Arctic-driven (S/NP3) changes in precipitation rates in autumn and early winter (September to December) between the SIC- and SIC+ years based on the 12 CMIP6 model ensemble. **e**, As in **d**, but for the Arctic-driven (S/NP3) changes in FFWI based on the 12 CMIP6 model ensemble. Stipples in **b-e** show regions that 2/3 CMIP6 models agree on the signs.

Figures

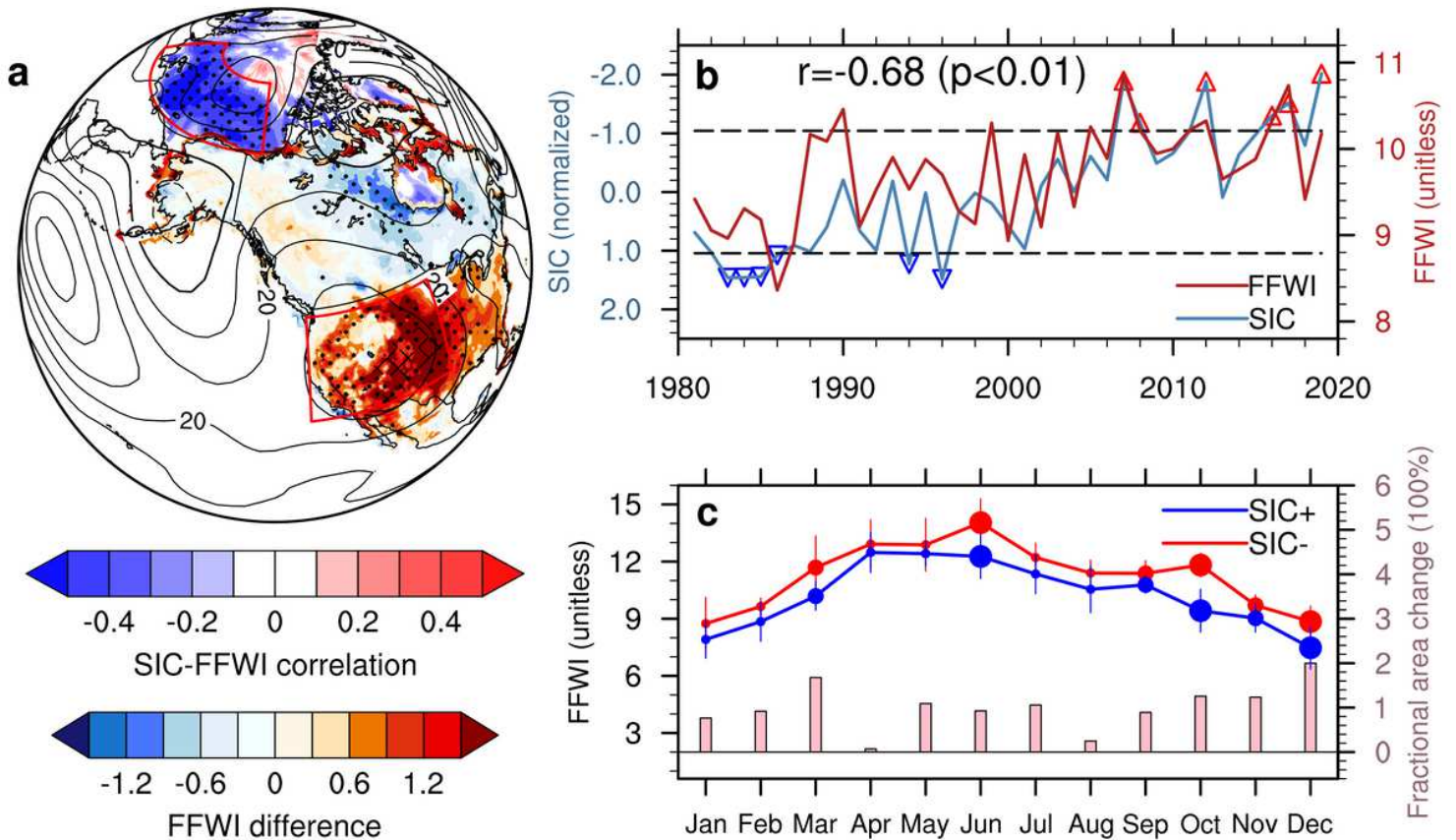


Figure 1

Observation- and reanalysis-based Arctic sea ice and regional fire teleconnection. a, spatial distributions of the correlation (shading in the Arctic) between seasonal average Arctic sea-ice concentrations in summer and autumn (July to October) and seasonal and regional average FFWI over the western U.S. in the following autumn and early winter (September to December), and the difference of seasonal average FFWI (shading in the U.S.) between years with minimum (SIC-: red up-pointing triangles in b) and maximum (SIC+: blue down-pointing triangles in b) Arctic SIC. The difference of seasonal (September to December) average geopotential height at 500 hPa between the SIC- and SIC+ years is also shown (contours with negative values in dashed lines; unit: m). b, time series of seasonal and regional average SIC (seasonal mean from July to October; normalized by its 1981-2010 climatological mean and standard deviation), FFWI (seasonal mean from September to December), and their correlation. The region definitions for the Pacific sector of the Arctic and the western U.S. are outlined by red boxes in a. The horizontal dashed lines denote the ± 1 standard deviations of normalized SIC as thresholds for selecting the SIC+/- years. c, the composite of monthly FFWI (solid lines with dots and error bars) and fractional burned area change of large wildfires (vertical bars) over the western U.S. Error bars in c denote ± 1 standard deviations of monthly FFWI in each group. Stipples in a mark regions that are significantly different from 0 at the 0.05 significance level of two-sided t-test, and hatching in a denotes statistically significant regions based on the stricter FDR method (see Methods) with local gridded p value

$\leq p_{FDR^*} = 0.0023$ at the threshold of $\alpha_{FDR} = 0.10$. Dot sizes for monthly FFWI in c denote the 0.05 (large) and 0.1 (medium) significance levels of two-sided t-test, respectively. Note: The designations employed and the presentation of the material on this map do not imply the expression of any opinion whatsoever on the part of Research Square concerning the legal status of any country, territory, city or area or of its authorities, or concerning the delimitation of its frontiers or boundaries. This map has been provided by the authors.

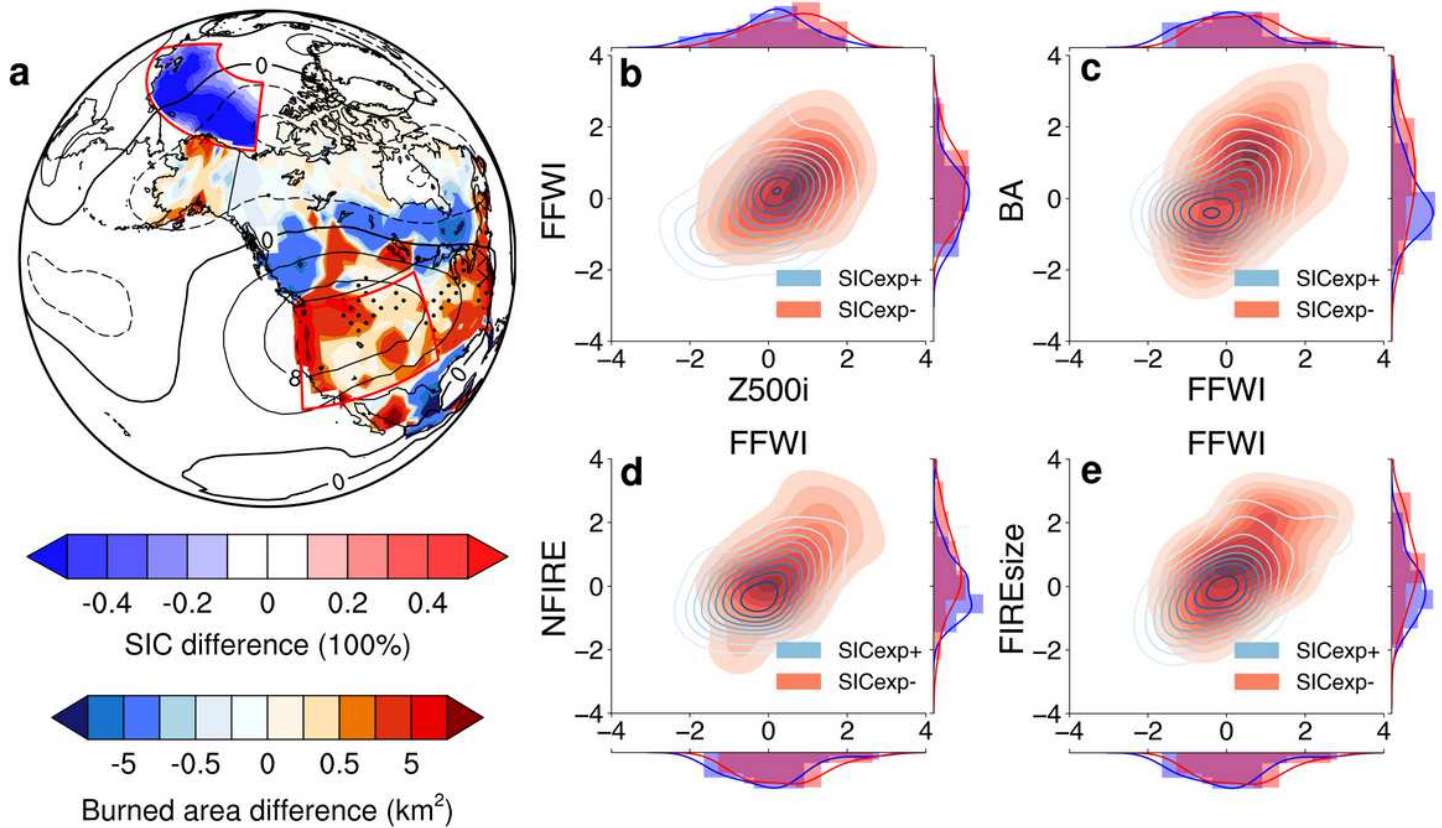


Figure 2

CESM-RESFire simulated Arctic sea ice and regional fire teleconnection. a, spatial distributions of the seasonal average (July to October) sea-ice concentration difference (color shading in the Arctic Ocean) between the SICexp- and SICexp+ experiments, and the seasonal average (September to December) burned area change (color shading in North America) in response to the sea-ice perturbation. The difference of Z500 between SICexp- and SICexp+ is also shown (contours with negative values in dashed lines; unit: m). b, 2-dimensional distributions of the seasonal mean fire-favorable circulation index (Z500i; standardized by first removing the 40-year mean and then normalizing by the standard deviation of Z500i from the SICexp+ experiment) and FFWI (also standardized by the 40-year mean and standard deviation of FFWI from the SICexp+ experiment) based on the kernel density estimation (KDE) for SICexp- (red shading) and SICexp+ (blue contours). 1-d KDE distributions for each index in SICexp- (red) and SICexp+ (blue) are also shown along the x- and y-axis. c, As in b, but for the comparison of standardized FFWI and regional burned area (BA). d, As in b, but for the comparison of standardized FFWI and regional mean fire count (NFIRE). e, As in b, but for the comparison of standardized FFWI and regional mean fire size

(FIREsize). Stipples in a show regions that are significantly different from 0 at the 0.1 significance level of two-sided t-test, and hatching in A denotes statistically significant regions based on the stricter FDR method (see Methods) with local gridded p value $\leq p_{FDR}^* = 0.017$ at the threshold of $\alpha_{FDR} = 0.20$. Note: The designations employed and the presentation of the material on this map do not imply the expression of any opinion whatsoever on the part of Research Square concerning the legal status of any country, territory, city or area or of its authorities, or concerning the delimitation of its frontiers or boundaries. This map has been provided by the authors.

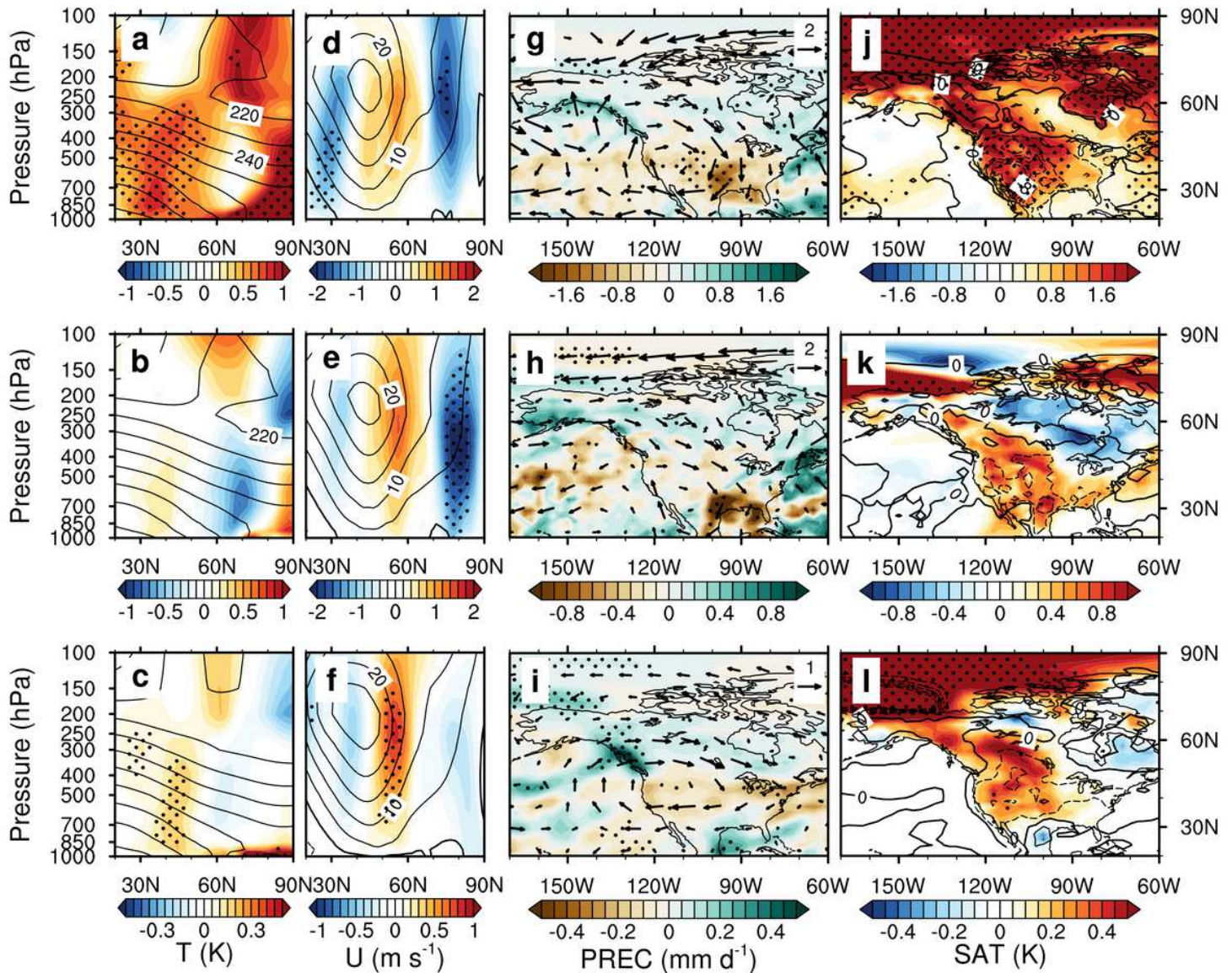


Figure 3

Physical processes underlying the Arctic sea ice and fire teleconnection. a, zonally-averaged (170 °W to 60 °W; as shown in g) temperature difference (shading) in autumn and early winter (September to December) between the SIC- and SIC+ years based on the original ERA5 reanalysis data. The time average of zonally-averaged temperature in the SIC+ years is also shown (contours; unit: K). b, As in a, but for the difference between the SICnotrd- and SICnotrd+ years based on the detrended ERA5 reanalysis data. c, As in a, but for the difference between the SICexp- and SICexp+ experiments based on the CESM-

RESFire simulations. d-f, As in a-c, but for zonally-averaged zonal wind based on the original ERA5 reanalysis data, the detrended ERA5 reanalysis data, and the CESM-RESFire simulations, respectively. g-i, As in a-c, but for wind circulation at 500 hPa (arrows; unit: m s⁻¹) and total precipitation rate (shading) differences based on the original ERA5 reanalysis data, the detrended ERA5 reanalysis data, and the CESM-RESFire simulations, respectively. j-l, As in a-c, but for 2-m relative humidity (contours with negative values in dashed lines; unit: %) and 2-m air temperature (shading) differences based on the original ERA5 reanalysis data, the detrended ERA5 reanalysis data, and the CESM-RESFire simulations, respectively. Stipples in a-l show regions that are significantly different from 0 at the 0.1 significance level of two-sided t-test. Note: The designations employed and the presentation of the material on this map do not imply the expression of any opinion whatsoever on the part of Research Square concerning the legal status of any country, territory, city or area or of its authorities, or concerning the delimitation of its frontiers or boundaries. This map has been provided by the authors.

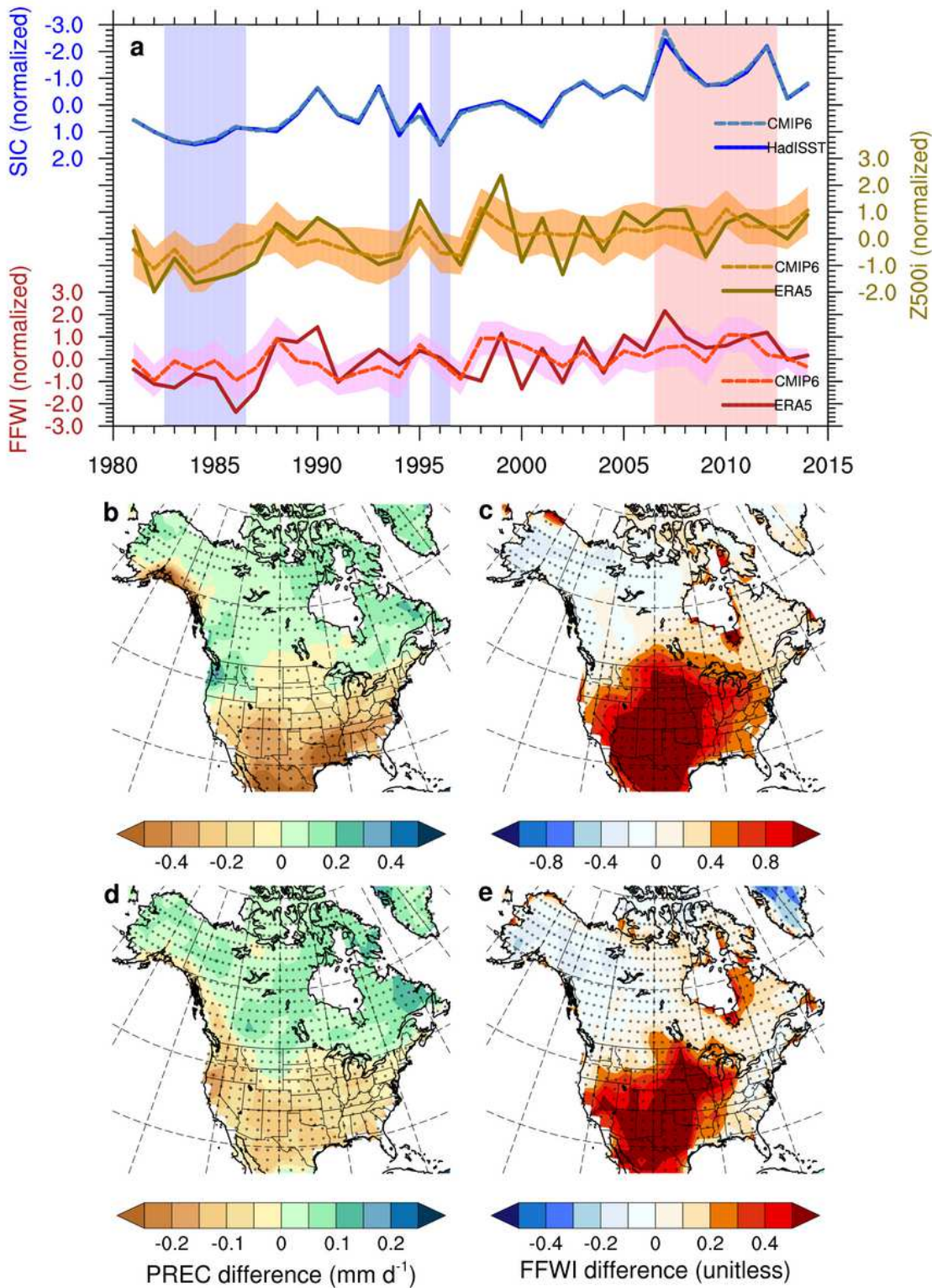


Figure 4

Arctic sea ice and regional fire weather teleconnection in the CMIP6 amip experiment. a, time series of normalized SIC, Z500i, and FFWI based on the observational/reanalysis data and 15 CMIP6 model ensemble. The shading along lines of the time series denotes ± 1 standard deviations of the model ensemble, and the vertical bar shading denotes years with minimum (pink; SIC-) and maximum (blue; SIC+) SIC for the composites in b and c. b, total changes in precipitation rates in autumn and early winter

(September to December) between the SIC- and SIC+ years based on the 12 CMIP6 model ensemble. c, As in b, but for total changes in FFWI. d, the Arctic-driven (S/NP3) changes in precipitation rates in autumn and early winter (September to December) between the SIC- and SIC+ years based on the 12 CMIP6 model ensemble. e, As in d, but for the Arctic-driven (S/NP3) changes in FFWI based on the 12 CMIP6 model ensemble. Stipples in b-e show regions that 2/3 CMIP6 models agree on the signs. Note: The designations employed and the presentation of the material on this map do not imply the expression of any opinion whatsoever on the part of Research Square concerning the legal status of any country, territory, city or area or of its authorities, or concerning the delimitation of its frontiers or boundaries. This map has been provided by the authors.

Supplementary Files

This is a list of supplementary files associated with this preprint. Click to download.

- [Supplementaryinformation.docx](#)